J. Mech. Phys. Solids 155 (2021) 104564

Contents lists available at ScienceDirect

Journal of the Mechanics and Physics of Solids

journal homepage: www.elsevier.com/locate/jmps

Microtwist homogenization of three-dimensional Pyrochlore lattices on zero modes and mechanical polarization

Rongyu Xia [a,b], Hussein Nassar [b], Hui Chen [b,*], Zheng Li [a], Guoliang Huang [b,*]

[a] State Key Laboratory for Turbulence and Complex Systems, Department of Mechanics and Engineering Science, College of Engineering, Peking University, Beijing 100871, PR China

[b] Department of Mechanical and Aerospace Engineering, University of Missouri, Columbia, MO 65211, USA

ARTICLE INFO

Keywords:
Microtwist continuum
Homogenization
Zero modes
Polarized mechanical metamaterials
3D Pyrochlore lattices

ABSTRACT

The mechanical Pyrochlore lattice was experimentally tested to demonstrate an intrinsically polar behavior of the material, which is soft on one side and hard on the opposite side (Bilal et al., 2017). The topological polarization in Pyrochlore lattices begs for developing a new effective medium theory because conventional Cauchy effective theories cannot predict the polarization phenomenon. In this study, we develop a 3D microtwist effective theory of Pyrochlore lattices to capture the P-asymmetric zero modes by which polarization emerges or fades on a macroscopic scale. By mapping three periodic zero modes to three macroscopic degrees of freedom, the 3D microtwist theory ends up being a kinematically enriched theory. The 3D microtwist elasticity is formulated by using two-scale asymptotic approach and its constitutive and balance equations are derived for a fairly generic isostatic lattice. Performance of the proposed theory is validated by the exact solution of the discrete model for reproducing zero modes and dispersion relations and quantitatively predicting asymmetric indentation responses. The study could shed lights on novel elastic theory of 3D polarized metamaterials outside the conventional framework of symmetry groups, which is never reported before.

1. Introduction

A mechanical lattice can be loosely defined as a web of beam or spring elements connecting a set of nodes or hinges. In design of the lattice material, harnessing of infinitesimal zero modes, deformation modes that cost little to no elastic energy, provides new paradigm to realize the nonstandard elastic behavior of the mechanical lattice (Lubensky et al., 2015). Although catastrophic in many scenarios, the presence of zero modes could be desired. The most spectacular application is the use of pentamode materials with five zero modes in acoustic cloaking (Milton and Cherkaev, 1995; Kadic et al., 2012; Norris and Shuvalov, 2011; Milton, 2013). Recently, polar materials with one intrinsic zero mode have been proposed in elastic cloaking (Nassar et al., 2018a, 2019, 2020a; Zhang et al., 2020; Xu et al., 2020). In those applications, zero modes appear and grow in the lattice material with Parity (P)-symmetry, namely the invariance of the set of solutions under the spatial inversion $\mathbf{x} \mapsto -\mathbf{x}$.

On the other hand, there are mechanical lattices or lattice materials with a broken P-symmetry, i.e., P-asymmetric, which refers to the fact that the space of solution is variant under the action of inversion $\mathbf{x} \mapsto -\mathbf{x}$. Materials with such property are polarized whose zero modes grow in amplitude in a preferential direction and decay in the opposite direction. Kagome lattices are one of the outstanding examples on topological polarization in isostatic lattices (Kane and Lubensky, 2014; Rocklin et al., 2017; Rocklin, 2017; Baardink et al., 2018; Ma et al., 2018; Mao and Lubensky, 2018; Zhang and Mao, 2018; Stenull and Lubensky, 2019; Nassar et al.,

* Corresponding authors.
E-mail addresses: hc6xc@mail.missouri.edu (H. Chen), huangg@misssouri.edu (G. Huang).

https://doi.org/10.1016/j.jmps.2021.104564
Received 5 March 2021; Received in revised form 24 June 2021; Accepted 8 July 2021
Available online 16 July 2021
0022-5096/Published by Elsevier Ltd.

Nomenclature

α_j, β_j	Bond spring constants
$\boldsymbol{\nabla}$, $\boldsymbol{\nabla}^{\mathrm{S}}$	Gradient and symmetrized gradient operators
$\boldsymbol{\rho}$, $\boldsymbol{\eta}$	Effective density tensor and moment of inertia tensor
$\boldsymbol{\sigma}$, $\boldsymbol{\xi}$, $\mathbf{s}$	Stress, Couple stress and hyperstress
$.'$	Conjugate transpose, adjoint
δ, δ^2	Prefixes for first and second order corrections
$\delta^2 K_H$	Next-nearest-neighbor spring constant
$\Delta_{\mathbf{e}_j}^{l_1,\ldots,l_6}$, $\Delta_{\mathbf{f}_j}^{l_1,\ldots,l_6}$	Bond elongations
ϵ, ϵ^*	Effective microtwist and Cauchy strain energy densities
γ	Similarity ratio
$\langle\cdot,\cdot\rangle$	The dot product
$(l_1,\ldots,l_6)$	Unit cell index
$\mathbf{C},\mathbf{B},\mathbf{D},\mathbf{M},\mathbf{A},\mathbf{Q}$	Effective constitutive tensors
$\mathbf{C}^*$	Effective Cauchy elasticity tensors
$\mathbf{e}_j$, $\mathbf{f}_j$	Unit vectors orienting the bonds
$\mathbf{F}$, $\boldsymbol{\tau}$	Resultant body force and torque
$\mathbf{I}$	Three-order identity tensor
$\mathbf{n}_k$	Unit normal vectors to the surfaces of a tetrahedron
$\mathbf{q}$, ω	Wavenumber and angular frequency
$\mathbf{r}_j$, $\mathbf{m}_j$	Dimensional and normalized lattice vectors
$\mathbf{t}_j^{l_1,\ldots,l_6}$, $\mathbf{I}_j^{l_1,\ldots,l_6}$	Internal and external nodal forces
$\mathbf{U}$, $\boldsymbol{\phi}$	Macroscopic fields of displacement and twisting
$\mathbf{U}_0$, $\boldsymbol{\phi}_0$	Translation and twisting amplitudes
$\mathbf{u}_k^{l_1,\ldots,l_6}$, $\mathbf{u}_k$	Displacement of node k
$\mathbf{x}_k^{l_1,\ldots,l_6}$, $\mathbf{x}_k$	Position of node k
Ω, $\partial\Omega$, $\mathbf{N}$	A domain, its boundary and the outward unit normal
$\boldsymbol{\Phi}$	Column vector of nodal displacements
a_j, b_j	Bond lengths
C_0, $C(\mathbf{q})$	Compatibility matrices
D, T	Mode shapes of translation and periodic twisting
h_k	The height of node k in the tetrahedron
$j = 1, 2, \ldots, 6$	Index of lattice vectors and bonds
K, M, C	Rigidity, mass and compatibility operators
$k = 1, 2, 3, 4$	Index of nodes
k_j	Equivalent spring constant
L	External forces column vector
m_k	Mass of node k
P_j, ∂_j	Unitary complex phase factor and partial derivative in direction $\mathbf{r}_j$
V	Volume of the unit cell
Z	Number of zero modes
z_j, $\mathbf{z}_j$	Distortion parameters and unit vectors orienting the distortion

2020b). For example, a regular Kagome lattice exhibits P-symmetry bulk zero modes which maintain uniform amplitude across the whole truss. However, general geometric distortions of the lattice will make zero modes polarized where the zero modes adopt exponential profiles that decay towards the bulk and re-localize at free boundaries. Kane and Lubensky (2014) characterized the conditions under which the re-localization of zero modes towards the free boundaries of a distorted lattice happens unevenly and favors certain boundaries over their opposites. Note that the resulting P-asymmetric distribution of zero modes are topological in nature which can be quantified by a topological polarization vector, so that they are immune to continuous perturbations, small and large, as long as the signs of distortion parameters remain unchanged. This is why such Kagome lattices are qualified as "topological polarization". The topological polarization leads to the appearance of elastic polarization effects whereby a finite sample appears hard when indented on one side and soft when indented on the opposite side. Elastic polarization effects are not restricted to boundaries and emerge in the bulk as well (Rocklin, 2017). Bilal et al. (2017) designed and tested a material made of 3D distorted Pyrochlore lattices featuring a polarized elastic behavior. A finite slab of their material appears soft when indented on one side

and hard when indented on the opposite side. To capture such zero modes on the level of the material requires finer measures of strain and its gradients. It is the purpose of the present paper to propose an enriched 3D effective medium theory capable of faithfully reproducing microstructural zero modes and related polarization effects on the continuum scale. Theoretical formulations are conducted for a fairly generic 3D truss: the Pyrochlore lattice.

Mechanical lattices with no zero modes have been successfully investigated using homogenization theory based on the Cauchy continuum mechanics (Deshpande et al., 2001; Hutchinson and Fleck, 2006). However, the polarization behavior due to P-asymmetric zero modes cannot be properly captured from the perspective of conventional continuum mechanics. To address this challenge, a Cosserat micropolar continuum (Cosserat and Cosserat, 1909) was suggested to model mechanical behavior of the polarized Kagome lattices by introducing both the vector displacement of nodes and the rotational degree of freedom (DOF) to describe microrotation (Sun et al., 2012). However, the material characteristic parameter of deformation comes into effect only when the deformation with non-negligible strain gradients or non-local effects is induced. Furthermore, the polarization effects in polarized Kagome or Pyrochlore lattices are caused by the accumulation of zero modes and are usually of a stronger dominant nature. Sun and Mao (2020) and Saremi and Rocklin (2020) proposed theories for polarized effective media of the strain gradient type. As a matter of fact, the polarization described by the micropolar elasticity and strain gradient theory is not of a topological nature and its effects are weak and restricted to boundary layers. By mapping each periodic zero mode to a macroscopic degree of freedom, we recently formulated a "bottom-up" higher-order theory baptized "microtwist" theory capable of rendering polarization effects of the 2D Kagome lattice on a macroscopic scale and quantitatively predicting the polarized indentation response of finite samples (Nassar et al., 2020b). In the study, the microtwist theory is systematically extended to study the mechanical polarization and related topological behavior of 3D pyrochlore lattices. To the best of our knowledge, little to no work has been conducted on realizing polarization effects in 3D topological materials.

Microtwist elasticity is the outcome of leading order two-scale asymptotic expansions with the displacement being a fast scale variable attached to the unit cell and the position being a slow variable attached to the structure in the long wavelength limit, $\mathbf{q} \to \mathbf{0}$. By progressively perturbing the geometry of regular Pyrochlore lattices so as to transform them into distorted ones, the total displacement field is composed of the macroscopic displacement field and of three additional DOFs, namely the twisting angles, directly related to microstructural zero modes. The resulting effective 3D Microtwist Continuum is therefore an enriched continuum allowing for the presence of periodic zero modes in the form of additional DOFs and the additional odd-order tensor elasticity constants are responsible for non-standard effects accompanying them such as polarization.

The structure of the paper is as follows. In Section 2, the compatibility and equilibrium relations of general Pyrochlore lattices are introduced. The classification in terms of regular and distorted Pyrochlore lattices is then recalled based on the number of periodic zero modes they support. In Section 3, the detailed derivation of the 3D microtwist continuum for the weakly-distorted Pyrochlore lattice is presented. In Section 4, dispersion relations and static phenomena taking place in regular and weakly-distorted Pyrochlore lattices are investigated. Results are derived from the discrete model of the Pyrochlore lattice, from the microtwist model and from Cauchy's model and then compared. The last section contains a brief conclusion.

2. Discrete modeling of Pyrochlore lattices and zero modes

General Pyrochlore lattices are introduced and classified into two phases, regular and distorted, based on the number and type of zero modes they support. The analysis here is based on the discrete lattice model. A continuum model, suitable for regular and weakly-distorted lattices, will be derived in the next section.

2.1. Compatibility and equilibrium equations

The Pyrochlore lattice shown in Fig. 1a is a 3D isostatic lattice made of a set of massless spring-like bonds connecting massive hinge-like nodes. A reference unit cell has hour nodes in the basis $\mathbf{x}_k$, $k \in \{1,2,3,4\}$, which constitute a tetrahedron composed of six bonds along the unit vectors $\mathbf{e}_j$ and of lengths a_j ($j \in \{1,2,3,4,5,6\}$); see Fig. 1b. The unit cell further has six other bonds along the unit vectors $\mathbf{f}_j$ and of lengths b_j. As such, lattice vectors $\mathbf{r}_j$ and unit vectors of bonds are related through

$$\begin{aligned} &\mathbf{r}_1 = a_1\mathbf{e}_1 - b_1\mathbf{f}_1, \quad \mathbf{r}_2 = a_2\mathbf{e}_2 - b_2\mathbf{f}_2, \quad \mathbf{r}_3 = a_3\mathbf{e}_3 - b_3\mathbf{f}_3, \\ &\mathbf{r}_4 = a_4\mathbf{e}_4 - b_4\mathbf{f}_4, \quad \mathbf{r}_5 = a_5\mathbf{e}_5 - b_2\mathbf{f}_5, \quad \mathbf{r}_6 = a_6\mathbf{e}_6 - b_6\mathbf{f}_6. \end{aligned} \tag{1}$$

Note that the bonds here are not arbitrarily prescribed. Indeed, one have $\mathbf{r}_1+\mathbf{r}_4-\mathbf{r}_2 = \mathbf{0}$, $\mathbf{r}_2+\mathbf{r}_5-\mathbf{r}_3 = \mathbf{0}$, $\mathbf{r}_3+\mathbf{r}_6-\mathbf{r}_1 = \mathbf{0}$, $\mathbf{r}_4+\mathbf{r}_5-\mathbf{r}_6 = \mathbf{0}$. Exterior to the unit cell, there are six other nodes with unnumbered solid green circles whose initial positions are given by $\mathbf{x}_1+\mathbf{r}_1$, $\mathbf{x}_1+\mathbf{r}_2$, $\mathbf{x}_1+\mathbf{r}_3$, $\mathbf{x}_2+\mathbf{r}_4$, $\mathbf{x}_3+\mathbf{r}_5$, $\mathbf{x}_4+\mathbf{r}_6$. Then the initial positions of all nodes can be deduced by translating along integer linear combination of the lattice vector $\mathbf{r}_j$. Thus the initial position of node k in unit cell $(l_1,\dots,l_6)$ reads

$$\mathbf{x}_k^{l_1,\dots,l_6} = \mathbf{x}_k + \mathbf{x}^{l_1,\dots,l_6} = l_1\mathbf{r}_1 + \cdots + l_6\mathbf{r}_6, \quad (l_1,\dots,l_6) \in \mathbb{Z}^6. \tag{2}$$

Pyrochlore lattices are isostatic lattices because the number of DOFs (4×3 = 12 possible displacements per unit cell) is equal to the number of bonds (12 springs oriented along the unit vectors $\mathbf{e}_j$ and $\mathbf{f}_j$). Thus, the compatibility relations between the displacement

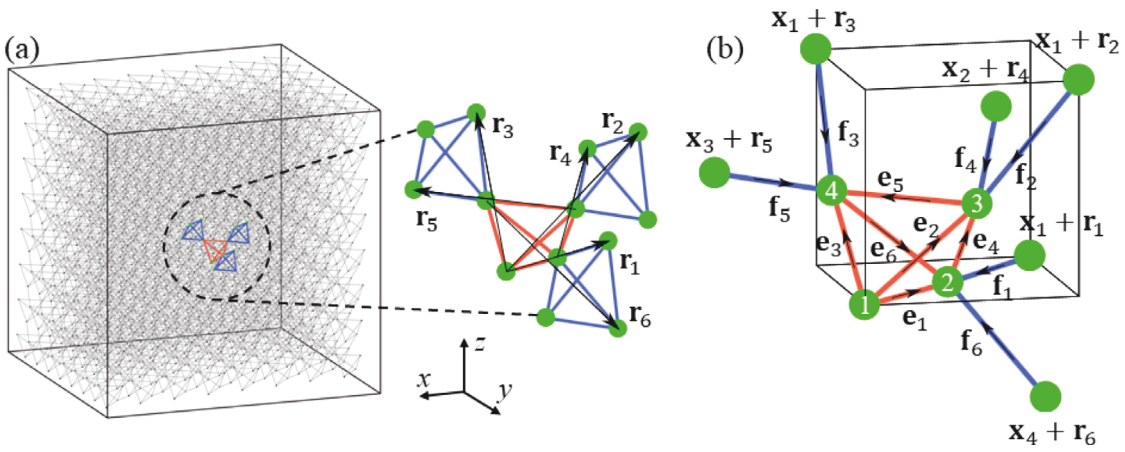

Fig. 1. A 3D Pyrochlore lattice: (a) a periodic reference configuration with six lattice vectors, $\mathbf{r}_j$, $j \in \{1,2,3,4,5,6\}$, and its animated version is shown in Supplementary Material, Video S1; (b) an annotated unit cell. The numbered and unnumbered solid green circles represent the interior and exterior masses of the unit cell respectively. Red bonds with unit vectors $\mathbf{e}_j$ and blue bonds with unit vectors $\mathbf{f}_j$ have respective lengths (a_j and b_j) and respective spring constants (α_j and β_j).

of mass k, $\mathbf{u}_k^{l_1,\dots,l_6}$, and the elongation of spring $\Delta_{\mathbf{e}_j}^{l_1,\dots,l_6}$ (resp. $\Delta_{\mathbf{f}_j}^{l_1,\dots,l_6}$) along $\mathbf{e}_j$ (resp. $\mathbf{f}_j$) are

$$
\begin{aligned}
\Delta_{\mathbf{e}_1}^{l_1,\dots,l_6} &= \left\langle \mathbf{e}_1, \mathbf{u}_2^{l_1,\dots,l_6} - \mathbf{u}_1^{l_1,\dots,l_6} \right\rangle, \quad \Delta_{\mathbf{f}_1}^{l_1,\dots,l_6} = \left\langle \mathbf{f}_1, \mathbf{u}_2^{l_1,\dots,l_6} - \mathbf{u}_1^{l_1+1,l_2,\dots,l_5,l_6} \right\rangle, \\
\Delta_{\mathbf{e}_2}^{l_1,\dots,l_6} &= \left\langle \mathbf{e}_2, \mathbf{u}_3^{l_1,\dots,l_6} - \mathbf{u}_1^{l_1,\dots,l_6} \right\rangle, \quad \Delta_{\mathbf{f}_2}^{l_1,\dots,l_6} = \left\langle \mathbf{f}_2, \mathbf{u}_3^{l_1,\dots,l_6} - \mathbf{u}_1^{l_1,l_2+1,l_3,\dots,l_6} \right\rangle, \\
\Delta_{\mathbf{e}_3}^{l_1,\dots,l_6} &= \left\langle \mathbf{e}_3, \mathbf{u}_4^{l_1,\dots,l_6} - \mathbf{u}_1^{l_1,\dots,l_6} \right\rangle, \quad \Delta_{\mathbf{f}_3}^{l_1,\dots,l_6} = \left\langle \mathbf{f}_3, \mathbf{u}_4^{l_1,\dots,l_6} - \mathbf{u}_1^{l_1,l_2,l_3+1,\dots,l_6} \right\rangle, \\
\Delta_{\mathbf{e}_4}^{l_1,\dots,l_6} &= \left\langle \mathbf{e}_4, \mathbf{u}_3^{l_1,\dots,l_6} - \mathbf{u}_2^{l_1,\dots,l_6} \right\rangle, \quad \Delta_{\mathbf{f}_4}^{l_1,\dots,l_6} = \left\langle \mathbf{f}_4, \mathbf{u}_3^{l_1,\dots,l_6} - \mathbf{u}_2^{l_1,\dots,l_4+1,l_5,l_6} \right\rangle, \\
\Delta_{\mathbf{e}_5}^{l_1,\dots,l_6} &= \left\langle \mathbf{e}_5, \mathbf{u}_4^{l_1,\dots,l_6} - \mathbf{u}_3^{l_1,\dots,l_6} \right\rangle, \quad \Delta_{\mathbf{f}_5}^{l_1,\dots,l_6} = \left\langle \mathbf{f}_5, \mathbf{u}_4^{l_1,\dots,l_6} - \mathbf{u}_3^{l_1,l_2,\dots,l_5+1,l_6} \right\rangle, \\
\Delta_{\mathbf{e}_6}^{l_1,\dots,l_6} &= \left\langle \mathbf{e}_6, \mathbf{u}_2^{l_1,\dots,l_6} - \mathbf{u}_4^{l_1,\dots,l_6} \right\rangle, \quad \Delta_{\mathbf{f}_6}^{l_1,\dots,l_6} = \left\langle \mathbf{f}_6, \mathbf{u}_2^{l_1,\dots,l_6} - \mathbf{u}_4^{l_1,l_2,\dots,l_5,l_6+1} \right\rangle.
\end{aligned}
\tag{3}
$$

For central forces, the tension in a spring is parallel to the spring orientation so that it is given by $\alpha_j \Delta_{\mathbf{e}_j}^{l_1,\dots,l_6} \mathbf{e}_j$ (resp. $\beta_j \Delta_{\mathbf{f}_j}^{l_1,\dots,l_6} \mathbf{f}_j$), where α_j (resp. β_j) is the spring constant along $\mathbf{e}_j$ (resp. $\mathbf{f}_j$). Thus, the equilibrium relations between the force on mass k, $\mathbf{t}_k^{l_1,\dots,l_6}$, and the spring tension are

$$
\begin{aligned}
\mathbf{t}_1^{l_1,\dots,l_6} =& \alpha_1 \Delta_{\mathbf{e}_1}^{l_1,\dots,l_6} \mathbf{e}_1 + \alpha_2 \Delta_{\mathbf{e}_2}^{l_1,\dots,l_6} \mathbf{e}_2 + \alpha_3 \Delta_{\mathbf{e}_3}^{l_1,\dots,l_6} \mathbf{e}_3 \\
&+ \beta_1 \Delta_{\mathbf{f}_1}^{l_1-1,\dots,l_6} \mathbf{f}_1 + \beta_2 \Delta_{\mathbf{f}_2}^{l_1,l_2-1\cdots,l_6} \mathbf{f}_2 + \beta_3 \Delta_{\mathbf{f}_3}^{l_1,l_2,l_3-1\cdots,l_6} \mathbf{f}_3, \\
\mathbf{t}_2^{l_1,\dots,l_6} =& -\alpha_1 \Delta_{\mathbf{e}_1}^{l_1,\dots,l_6} \mathbf{e}_1 + \alpha_4 \Delta_{\mathbf{e}_4}^{l_1,\dots,l_6} \mathbf{e}_4 - \alpha_6 \Delta_{\mathbf{e}_6}^{l_1,\dots,l_6} \mathbf{e}_6 \\
&- \beta_1 \Delta_{\mathbf{f}_1}^{l_1,\dots,l_6} \mathbf{f}_1 + \beta_4 \Delta_{\mathbf{f}_4}^{l_1,\dots,l_4-1,l_5,l_6} \mathbf{f}_4 - \beta_6 \Delta_{\mathbf{f}_6}^{l_1,\dots,l_6} \mathbf{f}_6, \\
\mathbf{t}_3^{l_1,\dots,l_6} =& -\alpha_2 \Delta_{\mathbf{e}_2}^{l_1,\dots,l_6} \mathbf{e}_2 - \alpha_4 \Delta_{\mathbf{e}_4}^{l_1,\dots,l_6} \mathbf{e}_4 + \alpha_5 \Delta_{\mathbf{e}_5}^{l_1,\dots,l_6} \mathbf{e}_5 \\
&- \beta_2 \Delta_{\mathbf{f}_2}^{l_1,\dots,l_6} \mathbf{f}_2 - \beta_4 \Delta_{\mathbf{f}_4}^{l_1,\dots,l_6} \mathbf{f}_4 + \beta_5 \Delta_{\mathbf{f}_5}^{l_1,\dots,l_5-1,l_6} \mathbf{f}_5, \\
\mathbf{t}_4^{l_1,\dots,l_6} =& -\alpha_3 \Delta_{\mathbf{e}_3}^{l_1,\dots,l_6} \mathbf{e}_3 - \alpha_5 \Delta_{\mathbf{e}_5}^{l_1,\dots,l_6} \mathbf{e}_5 + \alpha_6 \Delta_{\mathbf{e}_6}^{l_1,\dots,l_6} \mathbf{e}_6 \\
&- \beta_3 \Delta_{\mathbf{f}_3}^{l_1,\dots,l_6} \mathbf{f}_3 - \beta_5 \Delta_{\mathbf{f}_5}^{l_1,\dots,l_6} \mathbf{f}_5 + \beta_6 \Delta_{\mathbf{f}_6}^{l_1,\dots,l_6-1} \mathbf{f}_6.
\end{aligned}
\tag{4}
$$

Finally, the motion equation of the discrete Pyrochlore lattice reads

$$
\mathbf{t}_k^{l_1,\dots,l_6} + \mathbf{l}_k^{l_1,\dots,l_6} = m_k \ddot{\mathbf{u}}_k^{l_1,\dots,l_6},
\tag{5}
$$

where m_k is the mass k and $\mathbf{l}_k^{l_1,\dots,l_6}$ is an external force applied to the mass k of the unit cell $(l_1,\dots,l_6)$.

2.2. Periodic zero modes

Analyzing configurations where the various fields of interest vary slowly with respect to time and to the unit cell index $(l_1,\dots,l_6)$ is key to building an effective substitution medium for Pyrochlore lattices. By the same logic, it is expected that configurations that do not depend on time and on unit cell index $(l_1,\dots,l_6)$ at all will play a central role as well. These are referred to as *static periodic*

simplification and are investigated for the purpose of the classification of regular and distorted Pyrochlore lattices presented in this section.

By dismissing the dependence over unit cell index $(l_1, \dots, l_6)$, elongations are given by the matrix product

$$\Delta = \begin{bmatrix} \Delta_{\mathbf{e}_1} \\ \Delta_{\mathbf{e}_2} \\ \Delta_{\mathbf{e}_3} \\ \Delta_{\mathbf{e}_4} \\ \Delta_{\mathbf{e}_5} \\ \Delta_{\mathbf{e}_6} \\ \Delta_{\mathbf{f}_1} \\ \Delta_{\mathbf{f}_2} \\ \Delta_{\mathbf{f}_3} \\ \Delta_{\mathbf{f}_4} \\ \Delta_{\mathbf{f}_5} \\ \Delta_{\mathbf{f}_6} \end{bmatrix} = C_0 \begin{bmatrix} \mathbf{u}_1 \\ \mathbf{u}_2 \\ \mathbf{u}_3 \\ \mathbf{u}_4 \end{bmatrix}, \quad C_0 = \begin{bmatrix} -\mathbf{e}'_1 & \mathbf{e}'_1 & \mathbf{0} & \mathbf{0} \\ -\mathbf{e}'_2 & \mathbf{0} & \mathbf{e}'_2 & \mathbf{0} \\ -\mathbf{e}'_3 & \mathbf{0} & \mathbf{0} & \mathbf{e}'_3 \\ \mathbf{0} & -\mathbf{e}'_4 & \mathbf{e}'_4 & \mathbf{0} \\ \mathbf{0} & \mathbf{0} & -\mathbf{e}'_5 & \mathbf{e}'_5 \\ \mathbf{0} & \mathbf{e}'_6 & \mathbf{0} & -\mathbf{e}'_6 \\ -\mathbf{f}'_1 & \mathbf{f}'_1 & \mathbf{0} & \mathbf{0} \\ -\mathbf{f}'_2 & \mathbf{0} & \mathbf{f}'_2 & \mathbf{0} \\ -\mathbf{f}'_3 & \mathbf{0} & \mathbf{0} & \mathbf{f}'_3 \\ \mathbf{0} & -\mathbf{f}'_4 & \mathbf{f}'_4 & \mathbf{0} \\ \mathbf{0} & \mathbf{0} & -\mathbf{f}'_5 & \mathbf{f}'_5 \\ \mathbf{0} & \mathbf{f}'_6 & \mathbf{0} & -\mathbf{f}'_6 \end{bmatrix}, \tag{6}$$

where C_0 is a 12×12 compatibility matrix and a prime means conjugate transpose so that $\mathbf{e}'_k \mathbf{u}_k = \langle \mathbf{e}_k, \mathbf{u}_k \rangle$. Internal forces acting on four masses of the unit cell read

$$\begin{bmatrix} \mathbf{t}_1 \\ \mathbf{t}_2 \\ \mathbf{t}_3 \\ \mathbf{t}_4 \end{bmatrix} = -C'_0 K \Delta, \quad K = \mathrm{diag}(\alpha_1, \alpha_2, \alpha_3, \alpha_4, \alpha_5, \alpha_6, \beta_1, \beta_2, \beta_3, \beta_4, \beta_5, \beta_6), \tag{7}$$

where K is a diagonal matrix gathering the spring constants within one unit cell on its diagonal. Accordingly, the motion equation for periodic configurations can be expressed as

$$-C'_0 K C_0 \Phi + L = M \ddot{\Phi}, \quad \Phi = \begin{bmatrix} \mathbf{u}_1 \\ \mathbf{u}_2 \\ \mathbf{u}_3 \\ \mathbf{u}_4 \end{bmatrix}, \tag{8}$$

with $M = \mathrm{diag}\left(m_1 \mathbf{I}, m_2 \mathbf{I}, m_3 \mathbf{I}, m_4 \mathbf{I}\right)$ being the mass matrix, $\mathbf{I}$ being the 3×3 identity matrix, and where L is a column $\left(\mathbf{l}_1, \mathbf{l}_2, \mathbf{l}_3, \mathbf{l}_4\right)$ of external forces periodically applied to the masses of the lattice. Finally, dismissing dependence upon time yields the equilibrium equation for static periodic configurations

$$-C'_0 K C_0 \Phi + L = \mathbf{0}. \tag{9}$$

We then refer to Φ as a *periodic zero mode* when it is a free solution of the above equation, i.e., under $L = 0$. A periodic zero mode necessarily stores zero elastic energy

$$\sum_j \left(\alpha_j \Delta^2_{\mathbf{e}_j} + \beta_j \Delta^2_{\mathbf{f}_j} \right) = \Phi' C'_0 K C_0 \Phi = 0. \tag{10}$$

Accordingly, assuming all springs have strictly positive constants, a periodic zero mode deforms no springs and this translates into

$$C_0 \Phi = \mathbf{0}. \tag{11}$$

Hence, periodic zero modes are the null vectors of matrix C_0. Based on the rank-nullity theorem, their number is equal to $Z = 12 - \mathrm{rank}\, C_0$ where 12 is the dimension of C_0 and $\mathrm{rank}\, C_0$ its rank. By inspecting matrix C_0, there are only two possibilities: $(Z, \mathrm{rank}\, C_0) = (3, 9)$ or $(6, 6)$. If there exists a pair of surface planes along the tetrahedral surfaces are not aligned, then $Z = 3$ and C_0 is of rank 9. If for all j, $\mathbf{e}_j$ and $\mathbf{f}_j$ are colinear, then $Z = 6$ and C_0 is of rank 6. As a matter of fact, $\mathbf{e}_j$ and $\mathbf{f}_j$ being aligned and unitary meaning they are equal and opposite. We classify general Pyrochlore lattices based on this alternative. Lattices satisfying $Z = 3$ are the one we call *distorted*. These have no zero modes other than translations. Lattices with $Z = 6$ are the ones we call *regular*. They are characterized by any of the following equivalent properties:

- they satisfy the equation $\mathrm{rank}\, C_0 = 6$;
- their springs orientations along the tetrahedral edges are initially aligned in the sense $\mathbf{e}_j = \mathbf{f}_j$, for all j;
- they have six periodic zero modes.

The additional three periodic zero modes predicted in regular Pyrochlore lattices are hereafter referred to as "twisting" motions, which will be described next.

Global translations shown in Fig. 2 are characterized by $\mathbf{u}_1 = \mathbf{u}_2 = \mathbf{u}_3 = \mathbf{u}_4 = \mathbf{U}_o$ and take the matrix form

$$\Phi = \begin{bmatrix} \mathbf{U}_o \\ \mathbf{U}_o \\ \mathbf{U}_o \\ \mathbf{U}_o \end{bmatrix} = D \mathbf{U}_o, \quad D = \begin{bmatrix} \mathbf{I} \\ \mathbf{I} \\ \mathbf{I} \\ \mathbf{I} \end{bmatrix}, \tag{12}$$

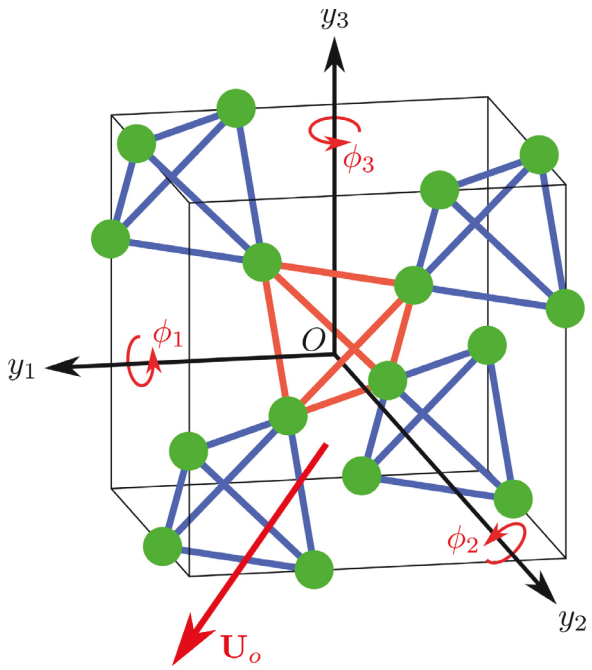

Fig. 2. Periodic zero modes of a regular Pyrochlore lattice: a linear combination of three global translations $\mathbf{U}_0$ and three global twisting motions, $\boldsymbol{\phi}_0 = [\phi_1, \phi_2, \phi_3]'$, around three orthogonal global axes y_j ($j \in \{1,2,3\}$). The origin of coordinates "O" is localized at the geometric center of the tetrahedron enclosed with red edges.

where $\mathbf{I}$ is the 3×3 identity matrix. It is easy to check that $C_0\boldsymbol{\Phi} = 0$. Translations span three periodic zero modes. For distorted lattices, they admit no other periodic zero modes besides translations. However, there exists three more periodic zero modes in regular lattices that can be described by the global twisting motions (ϕ_j, $j \in \{1,2,3\}$) around three orthogonal global axes y_1, y_2 and y_3, which take the form

$$\boldsymbol{\Phi} = \begin{bmatrix} \mathbf{T}_1 \\ \mathbf{T}_2 \\ \mathbf{T}_3 \\ \mathbf{T}_4 \end{bmatrix} \begin{bmatrix} \phi_1 \\ \phi_2 \\ \phi_3 \end{bmatrix} = T\boldsymbol{\phi}_o, \quad T = \begin{bmatrix} \mathbf{T}_1 \\ \mathbf{T}_2 \\ \mathbf{T}_3 \\ \mathbf{T}_4 \end{bmatrix}, \quad \boldsymbol{\phi}_o = \begin{bmatrix} \phi_1 \\ \phi_2 \\ \phi_3 \end{bmatrix}, \tag{13}$$

where

$$\mathbf{T}_k = \begin{bmatrix} A_1\mathbf{x}_k & A_2\mathbf{x}_k & A_3\mathbf{x}_k \end{bmatrix}, \quad A_m = \begin{bmatrix} 0 & -w_{m3} & w_{m2} \\ w_{m3} & 0 & -w_{m1} \\ -w_{m2} & w_{m1} & 0 \end{bmatrix}, \tag{14}$$

with w_{mn} ($m \in \{1,2,3\}$, $n \in \{1,2,3\}$) the component of the unit vector $\mathbf{w}_m$ along y_n. Here, the center of tetrahedron is chosen as the center of the twisting motion whereas $\boldsymbol{\phi}_o$ is the angle of rotation with respect to axes y_1, y_2, and y_3. Accordingly, the reference positions of the four interior masses, with respect to the origin, are

$$\begin{aligned} \mathbf{x}_1 &= \left(-a_1\mathbf{e}_1 - a_2\mathbf{e}_2 - a_3\mathbf{e}_3\right)/4, \\ \mathbf{x}_2 &= \left(3a_1\mathbf{e}_1 - a_2\mathbf{e}_2 - a_3\mathbf{e}_3\right)/4, \\ \mathbf{x}_3 &= \left(-a_1\mathbf{e}_1 + 3a_2\mathbf{e}_2 - a_3\mathbf{e}_3\right)/4, \\ \mathbf{x}_4 &= \left(-a_1\mathbf{e}_1 - a_2\mathbf{e}_2 + 3a_3\mathbf{e}_3\right)/4. \end{aligned} \tag{15}$$

T is indeed periodic zero modes because $C_0T = 0$. Therefore, the periodic zero modes of a regular Pyrochlore lattice are given by the linear combination of translations and twisting motions:

$$\boldsymbol{\Phi} = D\mathbf{U}_o + T\boldsymbol{\phi}_o. \tag{16}$$

3. Microtwist modeling of Pyrochlore lattices

An appropriate basis for periodic zero modes is introduced in the previous section, which greatly simplify the subsequent derivation of the macroscopic motion equation in this section. First, the distortion parameters controlling phase transitions

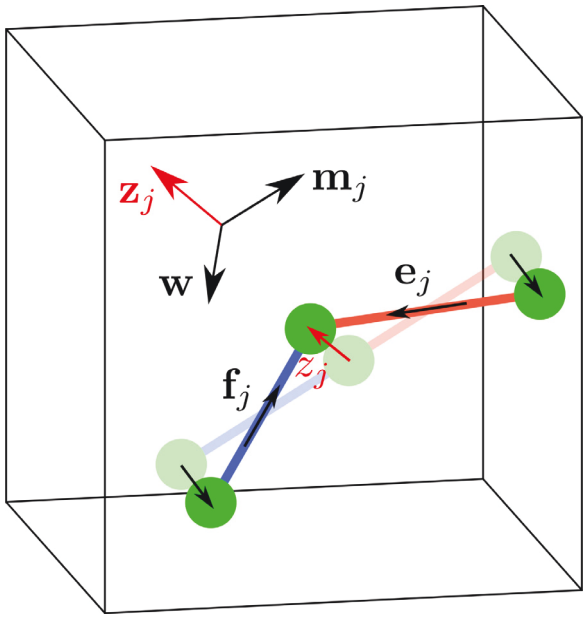

Fig. 3. Illustration of a phase transition from the regular (light color) to the distorted (deep color) lattice. If the vector of distortion parameter running from the regular configuration to the distorted one is in the same direction as $\mathbf{z}_j$, the distortion parameter z_j is positive and is negative otherwise. The only parameter relevant for our purpose are the elevations z_j, which could affect mechanical polarization effects in Pyrochlore lattices.

between regular and weakly-distorted Pyrochlore lattices are introduced. Next, the mechanics of Pyrochlore lattices are investigated asymptotically in the homogenization limit and in the critical regime corresponding to lattices on the brink of a regular-distorted phase transition. The effective medium is demonstrated to be a 3D microtwist continuum and closed-form expression of motion equations and constitutive relations are provided.

3.1. Perturbation theory

Starting with a regular Pyrochlore lattice, the initial positions of masses within a unit cell are perturbed: node j is displaced by z_j, see Fig. 3. The perturbation is expected to break the alignment of $\mathbf{e}_j$ and $\mathbf{f}_j$ so that the regular lattice becomes distorted in the sense of the classification of Section 2.2. Letting $(\mathbf{m}_j, \mathbf{z}_j)$ be an orthonormal basis where $\mathbf{m}_j$ is parallel to $\mathbf{r}_j$, and $\mathbf{z}_j$ is perpendicular to $\mathbf{m}_j$ that is defined as

$$\mathbf{z}_j = \left(\mathbf{m}_j \times \mathbf{w}\right) / \left\|\mathbf{m}_j \times \mathbf{w}\right\|, \tag{17}$$

where $\mathbf{w}$ is the unit vector parallel to $\mathbf{m}_1 + \mathbf{m}_2 + \mathbf{m}_3$. Here, we assume $\|z_j\| \ll \min(a_j, b_j)$ such that vectors $\mathbf{e}_j$ and $\mathbf{f}_j$ are now given by

$$\mathbf{e}_j = \mathbf{m}_j + \frac{z_j}{a_j}\mathbf{z}_j + O\left(\frac{z_j}{a_j}\right)^2, \quad \mathbf{f}_j = -\mathbf{m}_j + \frac{z_j}{b_j}\mathbf{z}_j + O\left(\frac{z_j}{b_j}\right)^2. \tag{18}$$

Two more explicit assumptions are then made in perturbation theory. One is that the displacements $\mathbf{u}_k^{l_1,\ldots,l_6}$ are assumed to derive from slowly varying smooth functions $\mathbf{u}_k(\mathbf{x})$ upon replacing $\mathbf{x}$ with $\mathbf{x}^{l_1,\ldots,l_6}$, where the position variable $\mathbf{x}$ is identified as a slow variable attached to the structure, while the displacement $\mathbf{u}_k$ is a fast scale variable attached to the unit cell in the long wavelength limit, $\mathbf{q} \to \mathbf{0}$. The relevant field variables are approximated by the leading-order Taylor expansions:

$$\begin{aligned}
\mathbf{u}_k^{l_1+1,\ldots,l_6} - \mathbf{u}_k^{l_1,\ldots,l_6} &= \partial_1 \mathbf{u}_k, \\
\mathbf{u}_k^{l_1,l_2+1,\ldots,l_6} - \mathbf{u}_k^{l_1,\ldots,l_6} &= \partial_2 \mathbf{u}_k, \\
\mathbf{u}_k^{l_1,l_2,l_3+1,\ldots,l_6} - \mathbf{u}_k^{l_1,\ldots,l_6} &= \partial_3 \mathbf{u}_k, \\
\mathbf{u}_k^{l_1,\ldots,l_4+1,l_5,l_6} - \mathbf{u}_k^{l_1,\ldots,l_6} &= \partial_4 \mathbf{u}_k, \\
\mathbf{u}_k^{l_1,\ldots,l_5+1,l_6} - \mathbf{u}_k^{l_1,\ldots,l_6} &= \partial_5 \mathbf{u}_k, \\
\mathbf{u}_k^{l_1,\ldots,l_6+1} - \mathbf{u}_k^{l_1,\ldots,l_6} &= \partial_6 \mathbf{u}_k,
\end{aligned} \tag{19}$$

where $\partial_j = \langle \mathbf{r}_j, \boldsymbol{\nabla} \rangle$ is the differential with respect to $\mathbf{x}$ in direction $\mathbf{r}_j$. The other assumption is that the displacements $\mathbf{u}_k^{l_1,\dots,l_6}$ are assumed to change with respect to time at small rates ω satisfying $\omega\sqrt{\max(m_k)} \ll \sqrt{\min(\alpha_j, \beta_j)}$.

Accordingly, in the homogenization limit, all three introduced perturbations are assumed to be infinitesimal and of the same order of magnitude. That is

$$\left\|\partial_j\right\| \sim \sqrt{\frac{\max(m_k)}{\min(\alpha_j, \beta_j)}}\omega \sim \frac{\left|z_j\right|}{\min(a_j, b_j)} \ll 1 \tag{20}$$

3.2. Asymptotic expansions

The second-order asymptotic expansions of the compatibility matrix are first introduced to rewrite the equations of the previous section. Injecting Eqs. (18) and (19) back into Eq. (3) yields

$$\begin{bmatrix} \Delta_{\mathbf{e}_1} \\ \Delta_{\mathbf{e}_2} \\ \Delta_{\mathbf{e}_3} \\ \Delta_{\mathbf{e}_4} \\ \Delta_{\mathbf{e}_5} \\ \Delta_{\mathbf{e}_6} \\ \Delta_{\mathbf{f}_1} \\ \Delta_{\mathbf{f}_2} \\ \Delta_{\mathbf{f}_3} \\ \Delta_{\mathbf{f}_4} \\ \Delta_{\mathbf{f}_5} \\ \Delta_{\mathbf{f}_6} \end{bmatrix} = C \begin{bmatrix} \mathbf{u}_1 \\ \mathbf{u}_2 \\ \mathbf{u}_3 \\ \mathbf{u}_4 \end{bmatrix} = C\boldsymbol{\Phi}, \quad C = C_0 + \delta C + \delta^2 C + \cdots, \tag{21}$$

The leading order term C_0 remains given by Eq. (6) and is rewritten as

$$C_0 = \begin{bmatrix} -\mathbf{m}_1' & \mathbf{m}_1' & \mathbf{0} & \mathbf{0} \\ -\mathbf{m}_2' & \mathbf{0} & \mathbf{m}_2' & \mathbf{0} \\ -\mathbf{m}_3' & \mathbf{0} & \mathbf{0} & \mathbf{m}_3' \\ \mathbf{0} & -\mathbf{m}_4' & \mathbf{m}_4' & \mathbf{0} \\ \mathbf{0} & \mathbf{0} & -\mathbf{m}_5' & \mathbf{m}_5' \\ \mathbf{0} & \mathbf{m}_6' & \mathbf{0} & -\mathbf{m}_6' \\ \mathbf{m}_1' & -\mathbf{m}_1' & \mathbf{0} & \mathbf{0} \\ \mathbf{m}_2' & \mathbf{0} & -\mathbf{m}_2' & \mathbf{0} \\ \mathbf{m}_3' & \mathbf{0} & \mathbf{0} & -\mathbf{m}_3' \\ \mathbf{0} & \mathbf{m}_4' & -\mathbf{m}_4' & \mathbf{0} \\ \mathbf{0} & \mathbf{0} & \mathbf{m}_5' & -\mathbf{m}_5' \\ \mathbf{0} & -\mathbf{m}_6' & \mathbf{0} & \mathbf{m}_6' \end{bmatrix}. \tag{22}$$

The first order correction $\delta C = \delta_z C + \delta_x C$ is composed of two terms. The first term is due to the perturbation that induces the regular-distorted phase transition:

$$\delta_z C = \begin{bmatrix} -z_1\mathbf{z}_1'/a_1 & z_1\mathbf{z}_1'/a_1 & \mathbf{0} & \mathbf{0} \\ -z_2\mathbf{z}_2'/a_2 & \mathbf{0} & z_2\mathbf{z}_2'/a_2 & \mathbf{0} \\ -z_3\mathbf{z}_3'/a_3 & \mathbf{0} & \mathbf{0} & z_3\mathbf{z}_3'/a_3 \\ \mathbf{0} & -z_4\mathbf{z}_4'/a_4 & z_4\mathbf{z}_4'/a_4 & \mathbf{0} \\ \mathbf{0} & \mathbf{0} & -z_5\mathbf{z}_5'/a_5 & z_5\mathbf{z}_5'/a_5 \\ \mathbf{0} & z_6\mathbf{z}_6'/a_6 & \mathbf{0} & -z_6\mathbf{z}_6'/a_6 \\ -z_1\mathbf{z}_1'/b_1 & z_1\mathbf{z}_1'/b_1 & \mathbf{0} & \mathbf{0} \\ -z_2\mathbf{z}_2'/b_2 & \mathbf{0} & z_2\mathbf{z}_2'/b_2 & \mathbf{0} \\ -z_3\mathbf{z}_3'/b_3 & \mathbf{0} & \mathbf{0} & z_3\mathbf{z}_3'/b_3 \\ \mathbf{0} & -z_4\mathbf{z}_4'/b_4 & z_4\mathbf{z}_4'/b_4 & \mathbf{0} \\ \mathbf{0} & \mathbf{0} & -z_5\mathbf{z}_5'/b_5 & z_5\mathbf{z}_5'/b_5 \\ \mathbf{0} & z_6\mathbf{z}_6'/b_6 & \mathbf{0} & -z_6\mathbf{z}_6'/b_6 \end{bmatrix}; \tag{23}$$

the second term is due to the fields being slowly varying in space:

$$\delta_x C = \begin{bmatrix} \mathbf{0} & \mathbf{0} & \mathbf{0} & \mathbf{0} \\ \mathbf{0} & \mathbf{0} & \mathbf{0} & \mathbf{0} \\ \mathbf{0} & \mathbf{0} & \mathbf{0} & \mathbf{0} \\ \mathbf{0} & \mathbf{0} & \mathbf{0} & \mathbf{0} \\ \mathbf{0} & \mathbf{0} & \mathbf{0} & \mathbf{0} \\ \mathbf{0} & \mathbf{0} & \mathbf{0} & \mathbf{0} \\ \mathbf{m}_1'\partial_1 & \mathbf{0} & \mathbf{0} & \mathbf{0} \\ \mathbf{m}_2'\partial_2 & \mathbf{0} & \mathbf{0} & \mathbf{0} \\ \mathbf{m}_3'\partial_3 & \mathbf{0} & \mathbf{0} & \mathbf{0} \\ \mathbf{0} & \mathbf{m}_4'\partial_4 & \mathbf{0} & \mathbf{0} \\ \mathbf{0} & \mathbf{0} & \mathbf{m}_5'\partial_5 & \mathbf{0} \\ \mathbf{0} & \mathbf{0} & \mathbf{0} & \mathbf{m}_6'\partial_6 \end{bmatrix}. \tag{24}$$

As for the second order correction of the compatibility matrix $\delta^2 C = \delta_z^2 C + \delta_x^2 C + \delta_{zx} C$, it turns out to be of no use for the following derivation.

The displacements are similarly expanded into

$$\boldsymbol{\Phi} = \boldsymbol{\Phi}_0 + \delta\boldsymbol{\Phi} + \delta^2\boldsymbol{\Phi} + \cdots, \tag{25}$$

where $\boldsymbol{\Phi}_0$ gathers the leading-order displacements, $\delta\boldsymbol{\Phi}$ and $\delta^2\boldsymbol{\Phi}$ are their first and second corrections respectively. Substituting the above expansions into the motion equation

$$-C'KC\boldsymbol{\Phi} + L = -\omega^2 M\boldsymbol{\Phi} \tag{26}$$

and keeping terms of the same order leads to a series of equations that can be solved iteratively. This is done next for the leading and first order equations. It is worth mentioning that L in Eq. (26) corresponds to body force and is taken to be slowly varying in space and of the same order of magnitude as inertial forces.

3.3. Leading and first order displacements

Keeping the leading order terms in the expansion of Eq. (26) yields

$$-C_0'KC_0\boldsymbol{\Phi}_0 = 0. \tag{27}$$

We have seen in Section 2.2 that the solution to this equation are periodic zero modes so that there exists translations $\mathbf{U}$ and twisting motions $\boldsymbol{\phi}$ such that

$$\boldsymbol{\Phi}_0 = D\mathbf{U} + T\boldsymbol{\phi}. \tag{28}$$

Keeping first order terms now implies

$$-C_0'KC_0\delta\boldsymbol{\Phi} + \Psi = 0, \quad \Psi = -C_0'K(\delta_x C + \delta_z C)(D\mathbf{U} + T\boldsymbol{\phi}). \tag{29}$$

Thus, $\delta\boldsymbol{\Phi}$ appears as a solution to a forced motion equation. Matrix C_0 being singular, the above equation admits solutions if and only if Ψ is balanced in the sense of being orthogonal to all zero modes:

$$D'\Psi = 0, \quad T'\Psi = 0. \tag{30}$$

Alternatively, Ψ is balanced if and only if it belongs to the range of matrix C_0', which in turn is identical to the range of matrix

$$G = \begin{bmatrix} G_1 & G_2 & G_3 & G_4 & G_5 & G_6 \end{bmatrix} \tag{31}$$

where

$$G_1 = \begin{bmatrix} -\mathbf{m}_1 \\ \mathbf{m}_1 \\ \mathbf{0} \\ \mathbf{0} \end{bmatrix}, \quad G_2 = \begin{bmatrix} -\mathbf{m}_2 \\ \mathbf{0} \\ \mathbf{m}_2 \\ \mathbf{0} \end{bmatrix}, \quad G_3 = \begin{bmatrix} -\mathbf{m}_3 \\ \mathbf{0} \\ \mathbf{0} \\ \mathbf{m}_3 \end{bmatrix},$$
$$G_4 = \begin{bmatrix} \mathbf{0} \\ -\mathbf{m}_4 \\ \mathbf{m}_4 \\ \mathbf{0} \end{bmatrix}, \quad G_5 = \begin{bmatrix} \mathbf{m} \\ \mathbf{0} \\ -\mathbf{m}_5 \\ \mathbf{m}_5 \end{bmatrix}, \quad G_6 = \begin{bmatrix} \mathbf{0} \\ \mathbf{m}_6 \\ \mathbf{0} \\ -\mathbf{m}_6 \end{bmatrix}, \tag{32}$$

given that $C_0' = \begin{bmatrix} G & -G \end{bmatrix}$. That is, Ψ is a balanced loading if and only if it reads

$$\Psi = G\psi, \quad \psi = \begin{bmatrix} \psi_1 \\ \psi_2 \\ \psi_3 \\ \psi_4 \\ \psi_5 \\ \psi_6 \end{bmatrix}, \tag{33}$$

where ψ_j are the generalized coordinates of Ψ along with G_j. Here, Ψ is indeed balanced and a straightforward calculation shows that

$$\psi = \begin{bmatrix} \beta_1 \langle \mathbf{m}_1 \partial_1, \mathbf{U} \rangle \\ \beta_2 \langle \mathbf{m}_2 \partial_2, \mathbf{U} \rangle \\ \beta_3 \langle \mathbf{m}_3 \partial_3, \mathbf{U} \rangle \\ \beta_4 \langle \mathbf{m}_4 \partial_4, \mathbf{U} \rangle \\ \beta_5 \langle \mathbf{m}_5 \partial_5, \mathbf{U} \rangle \\ \beta_6 \langle \mathbf{m}_6 \partial_6, \mathbf{U} \rangle \end{bmatrix} + \begin{bmatrix} (\gamma\beta_1 - \alpha_1) \langle z_1 \mathbf{z}_1, \mathbf{E}_1 \boldsymbol{\phi} \rangle \\ (\gamma\beta_2 - \alpha_2) \langle z_2 \mathbf{z}_2, \mathbf{E}_2 \boldsymbol{\phi} \rangle \\ (\gamma\beta_3 - \alpha_3) \langle z_3 \mathbf{z}_3, \mathbf{E}_3 \boldsymbol{\phi} \rangle \\ (\gamma\beta_4 - \alpha_4) \langle z_4 \mathbf{z}_4, \mathbf{E}_4 \boldsymbol{\phi} \rangle \\ (\gamma\beta_5 - \alpha_5) \langle z_5 \mathbf{z}_5, \mathbf{E}_5 \boldsymbol{\phi} \rangle \\ (\gamma\beta_6 - \alpha_6) \langle z_6 \mathbf{z}_6, \mathbf{E}_6 \boldsymbol{\phi} \rangle \end{bmatrix} + \begin{bmatrix} \beta_1 \langle \mathbf{m}_1 \partial_1, \mathbf{T}_1 \boldsymbol{\phi} \rangle \\ \beta_2 \langle \mathbf{m}_2 \partial_2, \mathbf{T}_1 \boldsymbol{\phi} \rangle \\ \beta_3 \langle \mathbf{m}_3 \partial_3, \mathbf{T}_1 \boldsymbol{\phi} \rangle \\ \beta_4 \langle \mathbf{m}_4 \partial_4, \mathbf{T}_2 \boldsymbol{\phi} \rangle \\ \beta_5 \langle \mathbf{m}_5 \partial_5, \mathbf{T}_3 \boldsymbol{\phi} \rangle \\ \beta_6 \langle \mathbf{m}_6 \partial_6, \mathbf{T}_4 \boldsymbol{\phi} \rangle \end{bmatrix} \tag{34}$$

where $\mathbf{E}_j = \begin{bmatrix} A_1 \mathbf{m}_j & A_2 \mathbf{m}_j & A_3 \mathbf{m}_j \end{bmatrix}$, and $\gamma = a_j / b_j$ is the j-independent similarity ratio.

Therefore, a solution $\delta\Phi$ exists and is given by

$$\delta\Phi = \Gamma\psi, \quad \Gamma = \begin{bmatrix} \Gamma_1 & \Gamma_2 & \Gamma_3 & \Gamma_4 & \Gamma_5 & \Gamma_6 \end{bmatrix}, \tag{35}$$

where Γ_j is a solution to

$$-C_0' K C_0 \Gamma_j + G_j = 0. \tag{36}$$

The Γ_j are straightforward to determine from the above equation, first by solving for $KC_0\Gamma_j$, then for $C_0\Gamma_j$ and finally for Γ_j. Skipping calculations, one finds that Γ is given by

$$\Gamma = \frac{1}{2} \begin{bmatrix} \frac{a_1/h_2}{\alpha_1+\beta_1}\mathbf{n}_2 & \frac{a_2/h_3}{\alpha_2+\beta_2}\mathbf{n}_3 & \frac{a_3/h_4}{\alpha_3+\beta_3}\mathbf{n}_4 & \frac{-a_4/h_3}{\alpha_4+\beta_4}\mathbf{n}_3 & \frac{-a_5/h_4}{\alpha_5+\beta_5}\mathbf{n}_4 & \frac{-a_6/h_2}{\alpha_6+\beta_6}\mathbf{n}_2 \\ \frac{-a_1/h_2}{\alpha_1+\beta_1}\mathbf{n}_2 & \frac{-a_2/h_3}{\alpha_2+\beta_2}\mathbf{n}_3 & \frac{-a_3/h_4}{\alpha_3+\beta_3}\mathbf{n}_4 & \frac{a_4/h_3}{\alpha_4+\beta_4}\mathbf{n}_3 & \frac{-a_5/h_4}{\alpha_5+\beta_5}\mathbf{n}_4 & \frac{-a_6/h_2}{\alpha_6+\beta_6}\mathbf{n}_2 \\ \frac{-a_1/h_2}{\alpha_1+\beta_1}\mathbf{n}_2 & \frac{-a_2/h_3}{\alpha_2+\beta_2}\mathbf{n}_3 & \frac{-a_3/h_4}{\alpha_3+\beta_3}\mathbf{n}_4 & \frac{-a_4/h_3}{\alpha_4+\beta_4}\mathbf{n}_3 & \frac{a_5/h_4}{\alpha_5+\beta_5}\mathbf{n}_4 & \frac{-a_6/h_2}{\alpha_6+\beta_6}\mathbf{n}_2 \\ \frac{-a_1/h_2}{\alpha_1+\beta_1}\mathbf{n}_2 & \frac{-a_2/h_3}{\alpha_2+\beta_2}\mathbf{n}_3 & \frac{-a_3/h_4}{\alpha_3+\beta_3}\mathbf{n}_4 & \frac{-a_4/h_3}{\alpha_4+\beta_4}\mathbf{n}_3 & \frac{-a_5/h_4}{\alpha_5+\beta_5}\mathbf{n}_4 & \frac{a_6/h_2}{\alpha_6+\beta_6}\mathbf{n}_2 \end{bmatrix}, \tag{37}$$

where $\mathbf{n}_k$ is the unit normal vector to the surface of the tetrahedron, $h_k = -\langle a_{k-1}\mathbf{m}_{k-1}, \mathbf{n}_k \rangle$ is the height of node $k = 2, 3, 4$ in the tetrahedron whose vertices are nodes 1, 2, 3, and 4. As a matter of fact, first order displacements can be modified by an addition of an arbitrary zero mode $D\delta\mathbf{U} + T\delta\boldsymbol{\phi}$. However, this term will play no further role and can be set to zero with no loss of generality.

3.4. Macroscopic motion equation

Keeping the second order terms in the expansion of Eq. (26) yields

$$\begin{aligned} &-C_0' K C_0 \delta^2\Phi - C_0' K(\delta_x C + \delta_z C)\delta\Phi - (\delta_x C + \delta_z C)' K C_0 \delta\Phi \\ &\quad - C_0' K \delta^2 C \Phi_0 - (\delta_x C + \delta_z C)' K(\delta_x C + \delta_z C)\Phi_0 + L = -\omega^2 M \Phi_0. \end{aligned} \tag{38}$$

Again, due to C_0 being singular, the above equation admits a solution if and only if the orthogonality conditions Eq. (30) are enforced. The first one reads

$$-D'(\delta_x C)' K C_0 \delta\Phi - D'(\delta_x C)' K(\delta_x C + \delta_z C)\Phi_0 + D' L = -\omega^2 D' M \Phi_0. \tag{39}$$

The second one is

$$-T'(\delta_x C + \delta_z C)' K C_0 \delta\Phi - T'(\delta_x C + \delta_z C)' K(\delta_x C + \delta_z C)\Phi_0 + T' L = -\omega^2 T' M \Phi_0. \tag{40}$$

Both equations involve the leading-order displacements spanned by translations $\mathbf{U}$ and twisting motions $\boldsymbol{\phi}$ and can be interpreted as a pair of macroscopic motion equations. Next, these equations will be rewritten in a form more suitable for interpretation, extract appropriate measures of strain and stress, and reveal the constitutive law that relates them.

3.5. Microtwist continuum

The quantities involved in (39) and (40) can be fully evaluated simply by injecting therein the derived expressions (12), (13), (22), (24), (23), (34), and (37). As a result, the macroscopic motion equations can be recast into the form

$$\begin{aligned} -\omega^2 (\boldsymbol{\rho} \cdot \mathbf{U} + \mathbf{d} \cdot \boldsymbol{\phi}) &= \mathbf{L} + \boldsymbol{\nabla} \cdot \left(\mathbf{C} : \boldsymbol{\nabla}^{\mathrm{S}} \mathbf{U} + \mathbf{B} : \boldsymbol{\nabla}\boldsymbol{\phi} + \mathbf{M} \cdot \boldsymbol{\phi} \right), \\ -\omega^2 \left(\mathbf{d}' \cdot \mathbf{U} + \boldsymbol{\eta} \cdot \boldsymbol{\phi} \right) &= \boldsymbol{\tau} + \boldsymbol{\nabla} \cdot \left(\mathbf{B}' : \boldsymbol{\nabla}^{\mathrm{S}} \mathbf{U} + \mathbf{D} : \boldsymbol{\nabla}\boldsymbol{\phi} + \mathbf{A} \cdot \boldsymbol{\phi} \right) \\ &\quad - \mathbf{M}' : \boldsymbol{\nabla}^{\mathrm{S}} \mathbf{U} - \mathbf{A}' \cdot \boldsymbol{\nabla}\boldsymbol{\phi} - \mathbf{Q} \cdot \boldsymbol{\phi}, \end{aligned} \tag{41}$$

where $\boldsymbol{\nabla}^{\mathrm{S}}$ is the symmetric gradient operator, $\boldsymbol{\nabla}\cdot$ is the divergence operator, and the dots $\cdot$ and : symbolize dot and double dot products, respectively. $\boldsymbol{\rho}$, $\boldsymbol{\eta}$, and $\mathbf{d}$ can be expressed as

$$\boldsymbol{\rho}=\frac{1}{V}\sum_{k=1,2,3,4} m_k\mathbf{I},\quad \boldsymbol{\eta}=\frac{1}{V}\sum_{k=1,2,3,4} m_k\mathbf{T}_k'\mathbf{T}_k,\quad \mathbf{d}=\frac{1}{V}\sum_{k=1,2,3,4} m_k\mathbf{T}_k, \tag{42}$$

where $V=-b_1b_2b_3\left(1+\gamma^3\right)\mathbf{m}_1\cdot\left(\mathbf{m}_2\times\mathbf{m}_3\right)$ is the volume of the unit cell.

The vector $\mathbf{L}$ is the resultant force acting on a unit cell per unit cell volume and $\boldsymbol{\tau}$ is the torque with respect to the geometric center O of the tetrahedron, which read

$$\mathbf{L}=\frac{1}{V}\sum_{k=1,2,3,4}\mathbf{l}_k,\quad \boldsymbol{\tau}=\frac{1}{V}\sum_{k=1,2,3,4}\mathbf{T}_k'\mathbf{l}_k. \tag{43}$$

The involved effective tensors are given by

$$\begin{aligned}
\mathbf{C}&=\frac{(1+\gamma)^2}{V}\sum_{j=1,2,3,4,5,6} b_j^2k_j\mathbf{m}_j\otimes\mathbf{m}_j\otimes\mathbf{m}_j\otimes\mathbf{m}_j,\\
\mathbf{B}&=\frac{(1+\gamma)^2}{V}\sum_{j=1,2,3,4,5,6} b_j^2k_j\mathbf{m}_j\otimes\mathbf{m}_j\otimes\mathcal{M}_j\otimes\mathbf{m}_j,\\
\mathbf{M}&=\frac{(1+\gamma)^2}{V}\sum_{j=1,2,3,4,5,6} z_jb_jk_j\mathbf{m}_j\otimes\mathbf{m}_j\otimes\left(\mathbf{E}_j'\mathbf{z}_j\right),\\
\mathbf{D}&=\frac{(1+\gamma)^2}{V}\sum_{j=1,2,3,4,5,6} b_j^2k_j\mathcal{M}_j\otimes\mathbf{m}_j\otimes\mathcal{M}_j\otimes\mathbf{m}_j,\\
\mathbf{A}&=\frac{(1+\gamma)^2}{V}\sum_{j=1,2,3,4,5,6} z_jb_jk_j\mathcal{M}_j\otimes\mathbf{m}_j\otimes\left(\mathbf{E}_j'\mathbf{z}_j\right),\\
\mathbf{Q}&=\frac{(1+\gamma)^2}{V}\sum_{j=1,2,3,4,5,6} z_j^2k_j\left(\mathbf{E}_j'\mathbf{z}_j\right)\otimes\left(\mathbf{E}_j'\mathbf{z}_j\right),\\
\mathbf{B}'&=\frac{(1+\gamma)^2}{V}\sum_{j=1,2,3,4,5,6} b_j^2k_j\mathcal{M}_j\otimes\mathbf{m}_j\otimes\mathbf{m}_j\otimes\mathbf{m}_j,\\
\mathbf{M}'&=\frac{(1+\gamma)^2}{V}\sum_{j=1,2,3,4,5,6} z_jb_jk_j\left(\mathbf{E}_j'\mathbf{z}_j\right)\otimes\mathbf{m}_j\otimes\mathbf{m}_j,\\
\mathbf{A}'&=\frac{(1+\gamma)^2}{V}\sum_{j=1,2,3,4,5,6} z_jb_jk_j\left(\mathbf{E}_j'\mathbf{z}_j\right)\otimes\mathcal{M}_j\otimes\mathbf{m}_j,
\end{aligned} \tag{44}$$

where $k_j=\alpha_j\beta_j/\left(\alpha_j+\beta_j\right)$, $\mathcal{M}_j=\mathbf{T}_1'\mathbf{m}_j$ for $j=1,2,3$ and $\mathcal{M}_j=\mathbf{T}_{j-2}'\mathbf{m}_j$ for $j=4,5,6$. Accordingly, only the fourth-order tensor $\mathbf{C}$ and the second-order tensor $\mathbf{Q}$ are completely symmetric, and the fourth-order tensor $\mathbf{D}$ maintains the major symmetry.

The macroscopic motion equations then can be written as the balance equations

$$-\omega^2(\boldsymbol{\rho}\cdot\mathbf{U}+\mathbf{d}\cdot\boldsymbol{\phi})=\mathbf{F}+\boldsymbol{\nabla}\cdot\boldsymbol{\sigma},\quad -\omega^2\left(\mathbf{d}'\cdot\mathbf{U}+\boldsymbol{\eta}\cdot\boldsymbol{\phi}\right)=\boldsymbol{\tau}+\boldsymbol{\nabla}\cdot\boldsymbol{\xi}+\boldsymbol{s}, \tag{45}$$

where $\boldsymbol{\sigma}$, $\boldsymbol{\xi}$ are second-order tensorial stress measures, and $\boldsymbol{s}$ is first-order tensorial stress measure, which related to the strain measures $\boldsymbol{\nabla}^{\mathrm{S}}\mathbf{U}$, $\boldsymbol{\nabla}\boldsymbol{\phi}$ and $\boldsymbol{\phi}$ through the macroscopic constitutive law

$$\begin{bmatrix}\boldsymbol{\sigma}\\ \boldsymbol{\xi}\\ -\boldsymbol{s}\end{bmatrix}=\begin{bmatrix}\mathbf{C} & \mathbf{B} & \mathbf{M}\\ \mathbf{B}' & \mathbf{D} & \mathbf{A}\\ \mathbf{M}' & \mathbf{A}' & \mathbf{Q}\end{bmatrix}\begin{bmatrix}\boldsymbol{\nabla}^{\mathrm{S}}\mathbf{U}\\ \boldsymbol{\nabla}\boldsymbol{\phi}\\ \boldsymbol{\phi}\end{bmatrix} \tag{46}$$

The boundary conditions suitable for the resolution of the balance equations over a finite domain Ω can be inferred by application of the divergence theorem. Calling $\mathbf{N}$ the normal to the boundary of Ω, it turns out then that either $\boldsymbol{\sigma}\cdot\mathbf{N}$ or $\mathbf{U}$ as well as $\boldsymbol{\xi}\cdot\mathbf{N}$ or $\boldsymbol{\phi}$ must be prescribed on the boundary Ω. Finally, a 3D microtwist continuum with extra DOFs and additional measures of strain, stress, and inertia have already been derived, which can describe the behavior of a general weakly-distorted Pyrochlore lattice in the homogenization limit.

Here, it is worth stressing that there is a significant difference between the proposed theory and the micropolar theory: the twisting angle $\boldsymbol{\phi}$ in Eq. (41) describes a relative motion of the unit cells, however, microrotation in the micropolar media is an absolute rotation. Therefore, the macroscopic dynamics described in Eq. (41) cannot be precisely captured by the micropolar theory. As a matter of fact, the microtwist medium can be understood as a particular Cosserat medium where the microrotation DOF $\boldsymbol{\phi}^{\mathrm{mr}}$ and infinitesimal rotation $\boldsymbol{\nabla}\times\mathbf{U}/2$ only appear in the combination $\boldsymbol{\phi}=\boldsymbol{\phi}^{\mathrm{mr}}-\boldsymbol{\nabla}\times\mathbf{U}/2$. Such a Cosserat medium would be unusual however as it would involve the second gradient of $\mathbf{U}$, specifically $\boldsymbol{\nabla}(\boldsymbol{\nabla}\times\mathbf{U})$, through $\boldsymbol{\nabla}\boldsymbol{\phi}$.

3.6. Influence of elasticity in the hinges

In the preceding derivations, nodal masses were assumed to behave like perfect hinges. The consequence is that variations of angles between the springs meeting at a given node cost no elastic energy at all. It could be of interest however to inspect the mechanics of Pyrochlore lattices with elastic hinges as they are expected to be better models of real structures.

Adding rotational springs so as to account for elasticity in the hinges is arguably equivalent to adding next-nearest-neighbor interactions between nodes. Both have a stabilizing effect on the lattice and will block twisting motions leaving translations as the only periodic zero modes. When the next-nearest-neighbor spring constants are comparable to or higher than the effective spring constants k_j, the Pyrochlore lattice will be far from the regular-distorted phase transition regime of interest. Here, the focus will be on lattices where the next-nearest-neighbor spring constants are much smaller than k_j, specifically, where they are of second-order compared to k_j since such lattices will be on the brink of a regular-distorted phase transition.

Formally, the expansion of the motion Eq. (38) will change so as to include an additional second-order term $C'_H\delta^2 K_H C_H \boldsymbol{\Phi}_0$ due to the presence of elasticity in the hinges. Therein, C_H is the periodic compatibility matrix corresponding to the next-nearest-neighbor bonds, which is shown in Appendix A, whereas $\delta^2 K_H$ is the corresponding diagonal matrix of elastic constants. This term is only relevant in the last step of the homogenization theory where the corrections $D'C'_H\delta^2 K_H C_H \boldsymbol{\Phi}_0$ and $T'C'_H\delta^2 K_H C_H \boldsymbol{\Phi}_0$ need to be added to the macroscopic motion equations. However, the former of these two corrections is zero, because of $C_H D = 0$, the translations remain periodic zero modes. Accordingly, the effective constitutive law remains the same as without elasticity in the hinges up to changing the effective parameter $\mathbf{Q}$ into

$$\mathbf{Q} = \boldsymbol{\kappa} + \frac{(1+\gamma)^2}{V} \sum_{j=1,2,3,4,5,6} z_j^2 k_j \left(\mathbf{E}'_j \mathbf{z}_j\right) \otimes \left(\mathbf{E}'_j \mathbf{z}_j\right), \tag{47}$$

with $\boldsymbol{\kappa} = T'C'_H\delta^2 K_H C_H T/V$.

The quadratic form of strain energy density ϵ is

$$\epsilon = \frac{\boldsymbol{\sigma} : \boldsymbol{\nabla}^{\mathrm{S}}\mathbf{U} + \boldsymbol{\xi} : \boldsymbol{\nabla}\boldsymbol{\phi} - \boldsymbol{s}\cdot\boldsymbol{\phi}}{2}, \tag{48}$$

where stresses are linear combinations of strains following the constitutive law of the microtwist continuum. Skipping calculations, its expression can be recast

$$\epsilon = \frac{1+\gamma}{2} \sum_j k_j \left[b_j \mathbf{m}_j \otimes \mathbf{m}_j : \boldsymbol{\nabla}^{\mathrm{S}}\mathbf{U} + b_j \mathcal{M}_j \otimes \mathbf{m}_j : \boldsymbol{\nabla}\boldsymbol{\phi} + z_j \langle \mathbf{E}'_j \mathbf{z}_j, \boldsymbol{\phi} \rangle \right]^2 + \frac{1}{2} \boldsymbol{\phi} \cdot \kappa \cdot \boldsymbol{\phi}, \tag{49}$$

where it is clear that it is non-negative. Definiteness however completely relies on the elastic constants k_j and κ being non-null. In particular, when the hinges are perfect ($\kappa = 0$), strain energy is semi-definite and therefore allows for microstructural zero modes to manifest on the macroscopic scale.

3.7. Parity symmetric in the 3D microtwist elasticity

Consider a homogeneous centrosymmetric domain Ω, i.e., such that $\mathbf{x} \in \Omega$ implies $-\mathbf{x} \in \Omega$. P-symmetry states that the space of solutions is invariant under the space inversion $\mathbf{x} \mapsto -\mathbf{x}$, i.e., $\boldsymbol{\Phi}(\mathbf{x}) = \boldsymbol{\Phi}(-\mathbf{x})$. Formally, P-symmetry is equivalent to the strain energy density ϵ being an even function of the gradient operator $\boldsymbol{\nabla}$. That is, the formal substitution $\boldsymbol{\nabla} \mapsto -\boldsymbol{\nabla}$ induced by the chain rule leaves the strain energy density as itself. While this property holds for Cauchy's strain energy density

$$\epsilon^* = \frac{1}{2} \boldsymbol{\nabla}^{\mathrm{S}}\mathbf{U} : \mathbf{C}^* : \boldsymbol{\nabla}^{\mathrm{S}}\mathbf{U}. \tag{50}$$

However, in general, P-symmetry does not hold for the microtwist strain energy density ϵ of Eq. (49). In fact,

$$\begin{aligned} \epsilon(\boldsymbol{\nabla}) = \frac{1+\gamma}{2} \sum_j k_j \left[b_j \mathbf{m}_j \otimes \mathbf{m}_j : \boldsymbol{\nabla}^{\mathrm{S}}\mathbf{U} + b_j \mathcal{M}_j \otimes \mathbf{m}_j : \boldsymbol{\nabla}\boldsymbol{\phi} + z_j \langle \mathbf{E}'_j \mathbf{z}_j, \boldsymbol{\phi} \rangle \right]^2 \\ + \frac{1}{2} \boldsymbol{\phi} \cdot \kappa \cdot \boldsymbol{\phi}, \\ \epsilon(-\boldsymbol{\nabla}) = \frac{1+\gamma}{2} \sum_j k_j \left[b_j \mathbf{m}_j \otimes \mathbf{m}_j : \boldsymbol{\nabla}^{\mathrm{S}}\mathbf{U} + b_j \mathcal{M}_j \otimes \mathbf{m}_j : \boldsymbol{\nabla}\boldsymbol{\phi} - z_j \langle \mathbf{E}'_j \mathbf{z}_j, \boldsymbol{\phi} \rangle \right]^2 \\ + \frac{1}{2} \boldsymbol{\phi} \cdot \kappa \cdot \boldsymbol{\phi}. \end{aligned} \tag{51}$$

Therefore, in the microtwist theory, a Pyrochlore lattice is P-symmetric if and only if all z_j vanish, i.e., if and only if the lattice is regular. Conversely, all distorted lattices, i.e., with at least one non-zero z_j, are P-asymmetric. And P-asymmetric lattices are referred to as polarized.

It is paramount to stress here that P-symmetry is different from and independent of material symmetry and the related notions of isotropy or anisotropy. For instance, regular equilateral pyrochlore lattices exhibit a non-zero fourth-order effective constitutive tensor B which breaks the material centrosymmetry of the constitutive law. Nonetheless, as pointed out earlier, regular lattices are P-symmetric.

In fact, observe how the rule $\boldsymbol{\nabla} \mapsto -\boldsymbol{\nabla}$ acts in the same manner as the rule $z_j \mapsto -z_j$ on the strain energy density ϵ. This means that the effective constitutive tensors responsible for P-asymmetry are the ones that are odd functions of the z_j. It can be concluded that the tensors $\mathbf{M}$ and $\mathbf{A}$, but not $\mathbf{B}$, are at the origin of macroscopic polarization effects in pyrochlore lattices.

3.8. Model reduction: Cauchy's continuum

Based on a kinematic hypothesis known as Cauchy–Born hypothesis, the displacements are the sum of one linear and one periodic field

$$\mathbf{u}_k^{l_1,\dots,l_6} = \mathbf{E}\cdot\mathbf{x}_j^{l_1,\dots,l_6} + \boldsymbol{\Delta}\mathbf{u}_k^{l_1,\dots,l_6}, \tag{52}$$

the linear part being the result of an imposed uniform macroscopic deformation $\mathbf{E}$. In doing so, the twisting gradients are precluded and the coupling trio $(\mathbf{B},\mathbf{D},\mathbf{A})$ is neglected. Our model reduces to Cauchy's continuum when this approximation is implemented.

As a matter of fact, when the strain and stress fields are uniform, the twisting gradient $\boldsymbol{\nabla\phi}$ is necessarily null and the static equilibrium simplifies into $\boldsymbol{s}=\mathbf{0}$. Solving for $\boldsymbol{\phi}$ entails $\boldsymbol{\phi}=-\mathbf{Q}^{-1}\cdot\mathbf{M}'\,:\,\boldsymbol{\nabla}^{\mathrm{S}}\mathbf{U}$ with $\mathbf{Q}\neq\mathbf{0}$. Finally, the reduced stress–strain relationship reads

$$\boldsymbol{\sigma}=\mathbf{C}^{*}\,:\,\boldsymbol{\nabla}^{\mathrm{S}}\mathbf{U},\quad \mathbf{C}^{*}=\mathbf{C}-\mathbf{M}\cdot\mathbf{Q}^{-1}\cdot\mathbf{M}'. \tag{53}$$

Using the elasticity tensor $\mathbf{C}^{*}$ is appealing as it greatly simplifies the constitutive law. Nonetheless, recall that its use is only justified for static uniform fields. Otherwise, the trio $(\mathbf{B},\mathbf{D},\mathbf{A})$ cannot be justifiably neglected. Taking this coupling into account will in fact significantly improve the quality of the predictions of the effective medium theory, various quantitative demonstrations are suggested in the following section.

4. Performance of the 3D microtwist medium

Having derived the equations of a microtwist continuum, it is natural to inquire whether that continuum is faithful in its predictions of the elastic behavior of different Pyrochlore lattices (regular and weakly-distorted). We first compare the dispersion diagrams from the lattice model of the Pyrochlore lattice, from the microtwist model and from Cauchy's model. We then investigate zero modes in finite Pyrochlore lattices so as to demonstrate their localization can also be quantitatively captured by the microtwist continuum. Last, we perform static indentation tests on two opposing faces of finite polarized Pyrochlore lattices to demonstrate large difference in their mechanical response and the emergence of mechanical polarization effects.

4.1. Prediction of dispersion relations

To study the unique static and dynamic properties of Pyrochlore lattices, we will focus on investigation of the first six fundamental wave branches based on the assumption of the microtwist theory. Considering in an infinite microtwist continuum under a plane wave in $\mathbf{x}$-direction, the translational displacement $\mathbf{U}$ and the twisting motion $\boldsymbol{\phi}$ are assumed to be the following form

$$\mathbf{U}(\mathbf{x},t)=\mathbf{U}_0\exp\left(i\langle\mathbf{q},\mathbf{x}\rangle-i\omega t\right),\quad \boldsymbol{\phi}(\mathbf{x},t)=\boldsymbol{\phi}_0\exp\left(i\langle\mathbf{q},\mathbf{x}\rangle-i\omega t\right). \tag{54}$$

Substituting the above equation in Eq. (41) and letting the resultant force–torque to be zero yields the dispersion equations. For comparison, we also obtain the dispersion equations for the Cauchy continuum modeling of Pyrochlore lattices by setting the twisting gradient $\boldsymbol{\nabla\phi}$ to be null and $\mathbf{s}$ to be zero. The 6-DOF ($\mathbf{U}$ and $\boldsymbol{\phi}$) microtwist continuum is then reduced to the 3-DOF ($\mathbf{U}$) Cauchy continuum.

In the following, numerical solutions based on the microtwist and Cauchy theories for two isostatic lattices (regular and weakly-distorted Pyrochlore lattices) will be conducted. For comparison, the exact dispersive solutions of the discrete lattice are also calculated. In the numerical examples, all springs are equal in length and in stiffness and all nodes are equal in mass, which here are all taken to the unity. The distortion parameters are zero for the regular lattice in Fig. 4a and $(z_1, z_2, z_3, z_4, z_5, z_6) = (0.074, 0.051, 0.088, 0.087, 0.062, 0.062)$ for the distorted lattice in Fig. 4b. The distorted lattice in this case is also mechanical polarized based on the topological theory (Stenull et al., 2016; Bilal et al., 2017). Figs. 4c and 4d show the dispersion curves of the regular and distorted lattices, respectively. For the Cauchy continuum, there are only three branches of the dispersion curves corresponding translational waves. However, the microtwist continuum can produce six branches corresponding the coupled translational and rotational waves. Moreover, it agrees well with those given by the discrete lattice model and a discrepancy between the microtwist and Cauchy models is found in a relative higher frequency regime. From Fig. 4c, it is worth mentioning that the microtwist continuum is able to accurately capture the zero modes. However, the conventional Cauchy theory is totally failure to capture zero modes. The quantitatively characterization of zero modes will be illustrated in the following section.

4.2. Continuum characterization of zero modes

For the microtwist continuum, zero modes can be represented by the condition of zero strain energy over a domain Ω, i.e., $\int_{\Omega}\epsilon=0$, as

$$b_j\mathbf{m}_j\otimes\mathbf{m}_j\,:\,\boldsymbol{\nabla}^{\mathrm{S}}\mathbf{U}+b_j\mathcal{M}_j\otimes\mathbf{m}_j\,:\,\boldsymbol{\nabla\phi}+z_j\left(\mathbf{E}_j'\mathbf{z}_j\right)\cdot\boldsymbol{\phi}=0,\quad j=1,\dots,6. \tag{55}$$

The above system of linear partial differential equations provides a continuum characterization of the zero modes of Pyrochlore lattices. The system is independent of the elastic moduli k_j, which represents the configurations that do not stretch any springs.

In the following, we perform modal analyses of the above system to investigate location or distribution of zero modes in terms of the translational displacements in the same regular and weakly-distorted lattices as before. We then quantitatively compare the

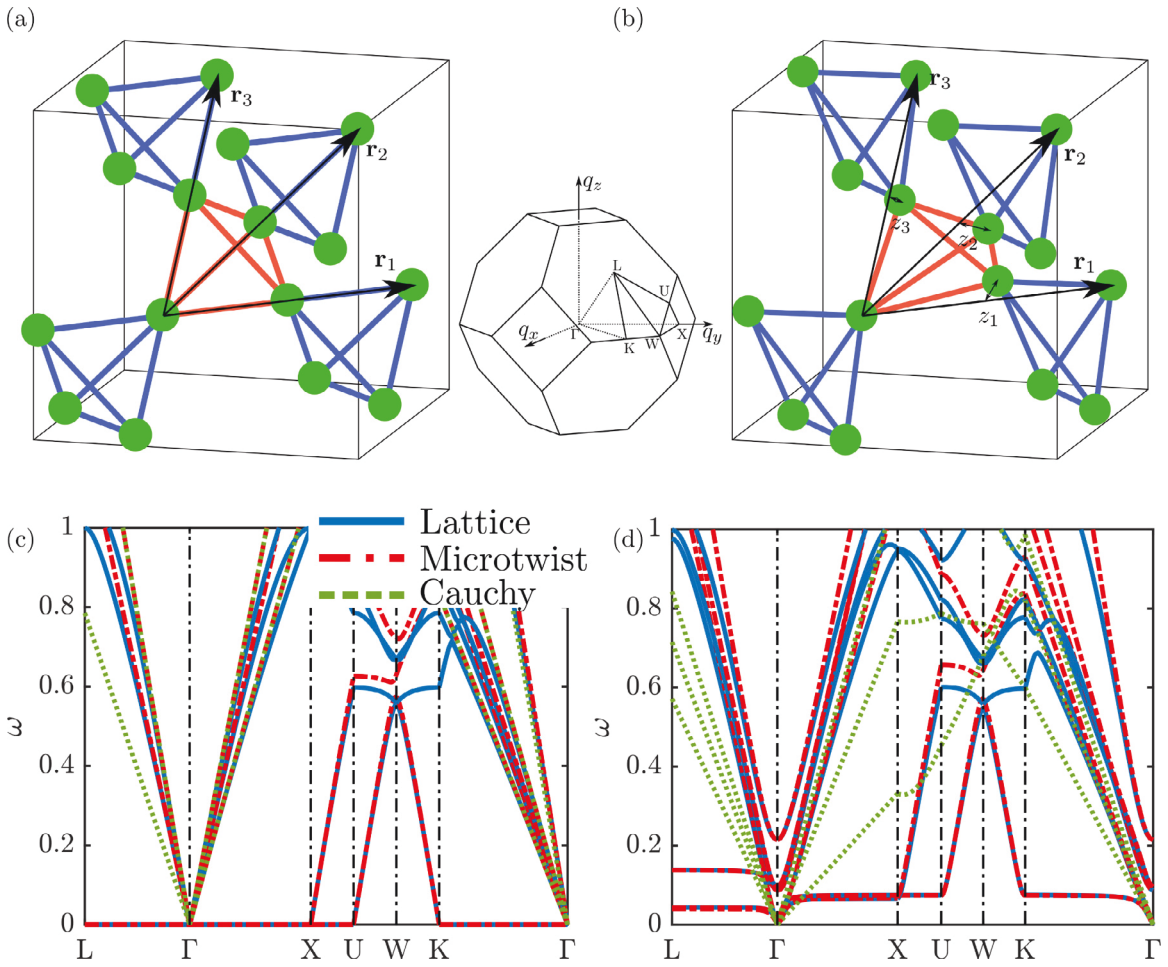

Fig. 4. Example of regular (a) and distorted (b) Pyrochlore lattices, and of their respective dispersion diagrams (c) and (d). Blue solid, red dashed and green dotted lines correspond to the dispersion relations of the discrete lattices, microtwist and Cauchy models respectively. The inset shows the first Brillouin zone with symmetry points.

prediction from the discrete lattice model with 13 × 13 × 13 unit cells (Figs. 5a and 5b) and the microtwist continuum model (Figs. 5c and 5d) under free boundary conditions on both top and bottom surfaces but Dirichlet boundary conditions on others surfaces. In the simulation, it is more convenient to obtain approximate zero modes by minimizing strain energy in the presence of a small residual elastic energy stored in the hinges (i.e., for $0 < \kappa \sim 0$). Three components corresponding to U_x, U_y, and U_z are extracted from the eigenmode of lowest energy and are plotted as normalized color maps in Fig. 5. In the two cases, the microtwist continuum predicts well the mode shape of the approximate zero modes: the regular lattice only has bulk modes (Figs. 5a and 5c); the polarized lattice has P-asymmetric zero modes where the surface modes are localized on the top surface while deserting the bottom surface (Figs. 5b and 5d). The emergence of the asymmetric behavior is due to the intrinsic polarization effects in the polarized lattice. It should be noted that all of the above results agree with the observation made by the topological theory (Stenull et al., 2016) and the experimental measurements (Bilal et al., 2017) as well.

In fact, the P-asymmetric distribution of zero modes in Pyrochlore lattices is size-dependent. In order to validate this, numerical simulations are then performed to illustrate the scaling effect. In the simulation, the polarized Pyrochlore lattice with fixed dimensions is composed of a total of $N_x \times N_y \times N_z$ unit cells. The number of unit cells $N = N_x = N_y = N_z$ are adjusted with 9, 13, 17 and 21 to change the unit cell sizes. Here, the angles between tetrahedrons are the same as the polarized lattice in Fig. 4b, while the spring stiffness is proportional to the edge length of tetrahedron. We apply the same boundary conditions as in Fig. 5, and then conduct modal analyses to calculate the zero modes for both the discrete and continuum models. Fig. 6 illustrates one component corresponding to U_z in the normalized color map. It is observed that with the decrease of the unit cell size, the zero modes are accumulated closer to the top surface and its penetration depth into the bulk lattice is reduced. In this sense, the P-asymmetric behavior is topologically protected and will not disappear with the change of the unit cell size.

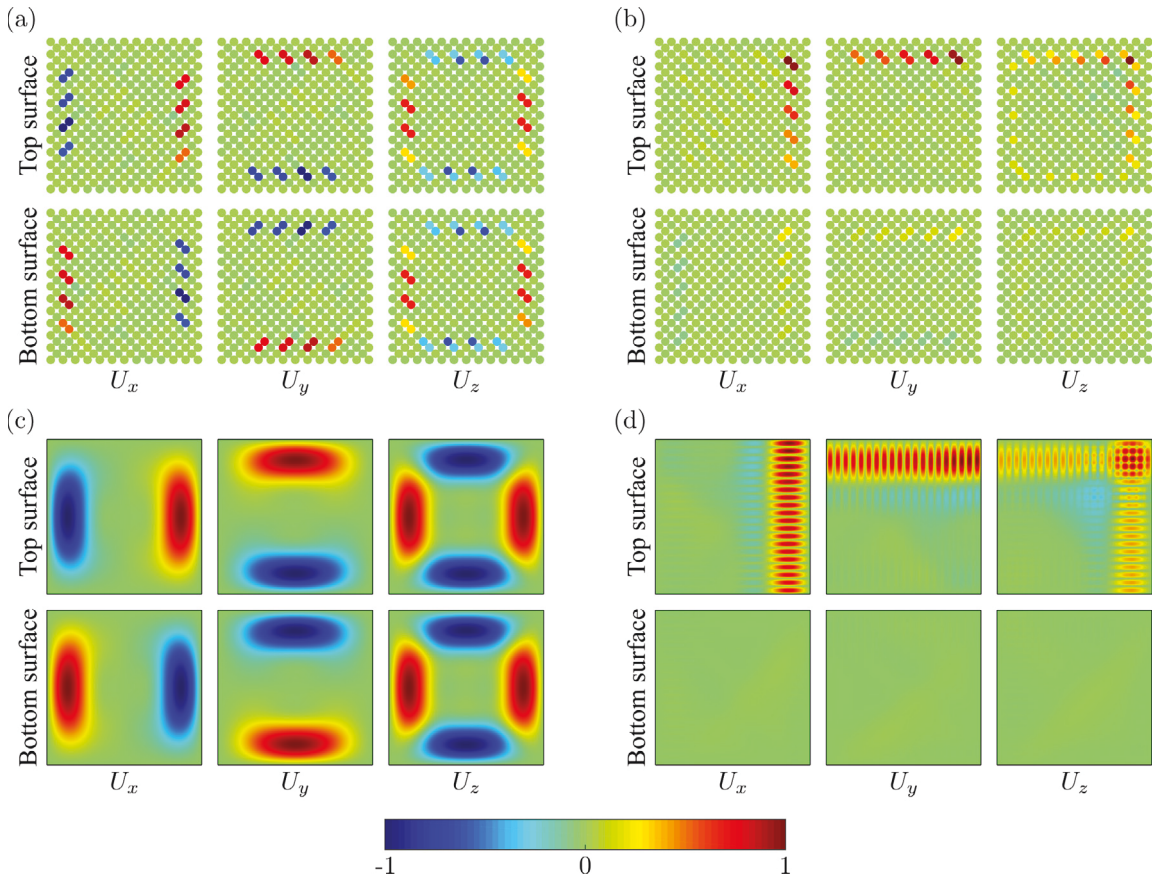

Fig. 5. Modal analyses of regular (a, c) and polarized (b, d) Pyrochlore lattices and of their respective zero modes by employing the discrete lattice model (a, b) and the microtwist continuum model (c, d).

4.3. Asymmetric indentation responses

We are now ready to perform indentation tests so as to access polarization behavior of polarized Pyrochlore lattices. Consider a cubic sample ($13 \times 13 \times 13$ unit cells) where the bottom surface is fixed and the top surface is applied by a point inward force **F**, as shown in Fig. 7a. Fig. 7(b) presents the displacement profiles of the regular and polarized lattice calculated by microtwist continuum. The displacement U_x, U_y, and U_z of the regular lattice are symmetrically distributed. However, in the case of the polarized lattice, all the displacement components are no longer symmetrically distributed. Figs. 7c and 7d show the displacement fields of the middle section of regular and polarized pyrochlore lattices, respectively. It should be interesting to mention that the microtwist continuum theory can quantitatively capture dominant polarization effects that penetrate deep into the bulk of the lattice or material.

To quantitatively investigate the asymmetric indentation responses, we calculate the displacement U_z at the same point where the force is applied and plot the response of each two opposite faces in Fig. 8, which shows the excellent agreement between the lattice model and the microtwist model. In the case of regular lattice, the elastic responses on the top surface, $(0, 0, 1)$, and the bottom surface, $(0, 0, -1)$ are the same. In the case of polarized lattice, for the two opposite surfaces, the elastic responses to the same compression load are very different and keep diverging with increasing indentation value. This provides an numerical evidence of the realization of a 3D mechanical polarized lattice with an asymmetric elastic response.

At last, in order to quantitatively illustrate the unit cell size effects on polarized mechanical behavior, indentation tests are then performed on the Pyrochlore lattices of different number of unit cells. Fig. 9 shows the normalized displacement at the top and bottom surfaces with the change of the unit cell sizes. From the figure, it first can be seen that the top surface, $(0, 0, 1)$, is always harder than the bottom one, $(0, 0, -1)$, which means the polarization behavior is robust against the unit cell size. Second, the top surface becomes softer and the bottom surface becomes harder with the decrease of the unit cell sizes, which is due to the redistribution of zero modes with the change of the unit size as illustrated in Fig. 6. It is interesting to note that with the decrease of the unit cell size, the hardness of bottom surface can be reduced to the one described by the Cauchy continuum theory that is size-independent.

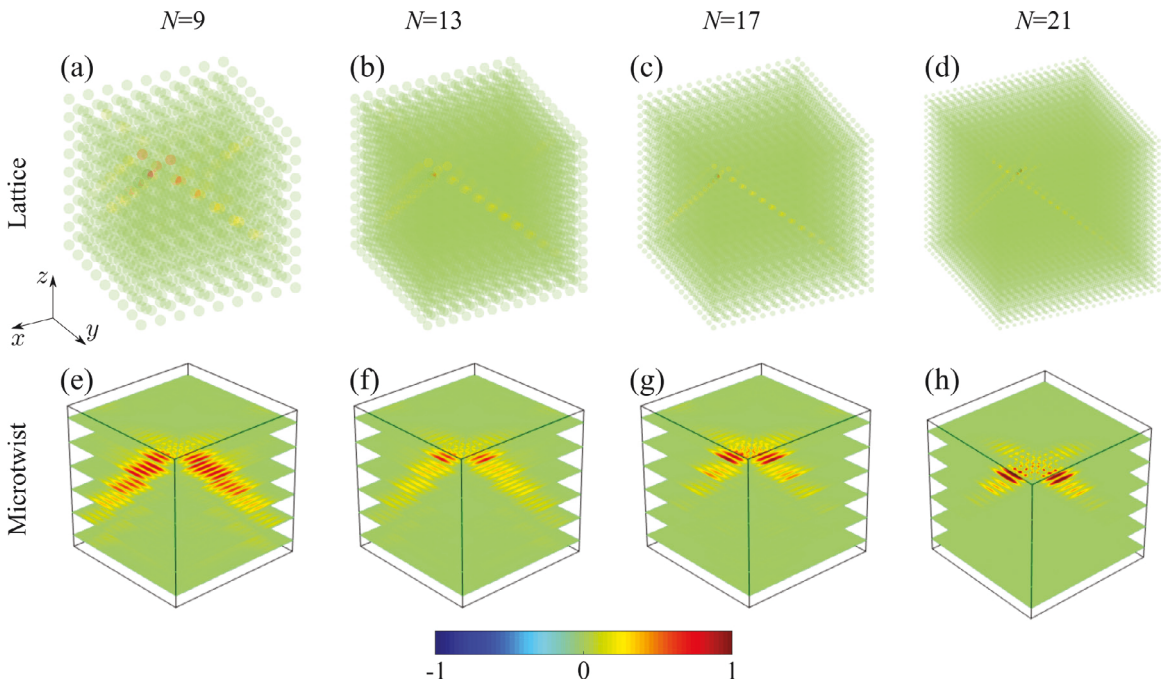

Fig. 6. Zero modes of the polarized Pyrochlore lattice by employing the discrete lattice model and (a–d) the microtwist continuum model (e–h) with the number of unit cells $N = 9, 13, 17, 21$ along each dimension.

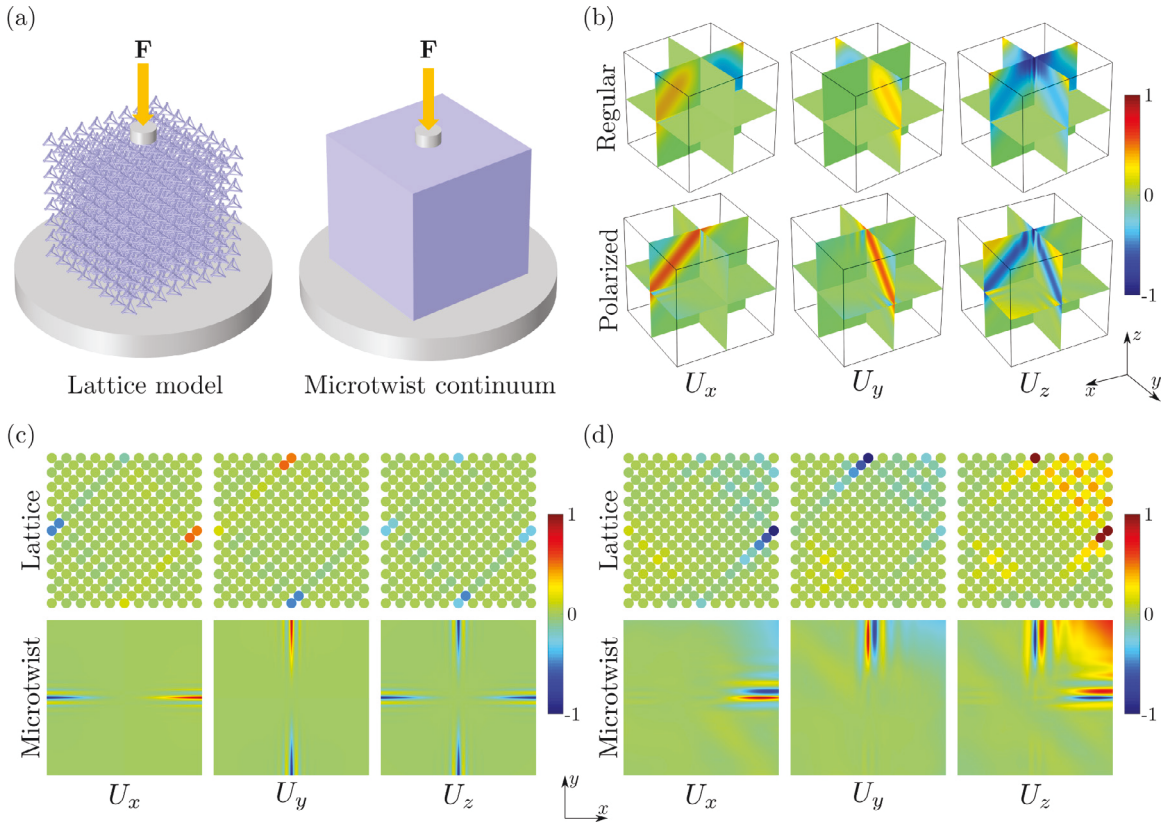

Fig. 7. Simulated elastic fields of Pyrochlore lattices under top-indentation: (a) Schematic representation of the numerical setup for the lattice model and the microtwist model; (b) displacement profiles of the regular Pyrochlore lattice and the Polarized Pyrochlore lattice calculated by the microtwist model; (c, d) displacement profiles of the middle section of the regular lattice (c) and the distorted lattice (d).

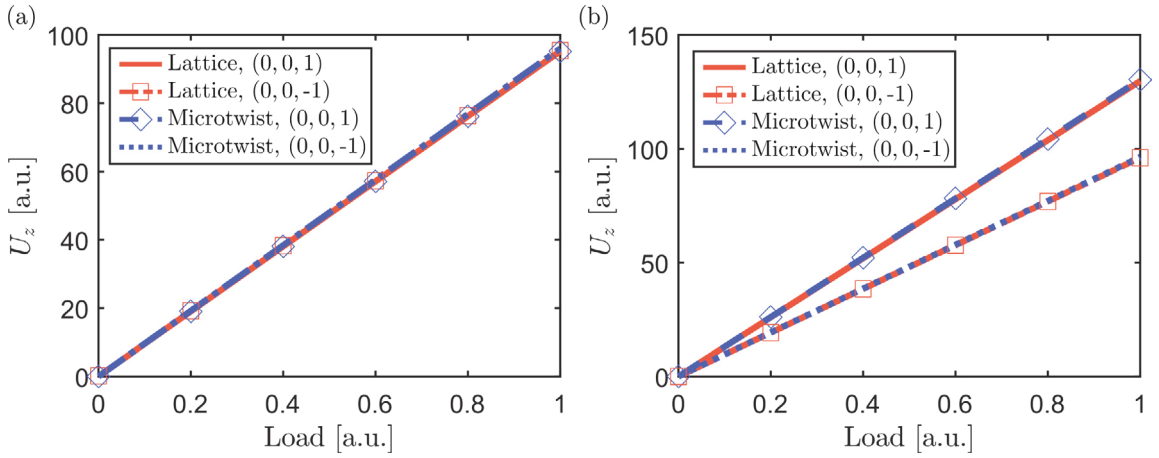

Fig. 8. Simulated indentation responses of the surface of Pyrochlore lattices along z axis: (a) regular lattice; (b) polarized lattice.

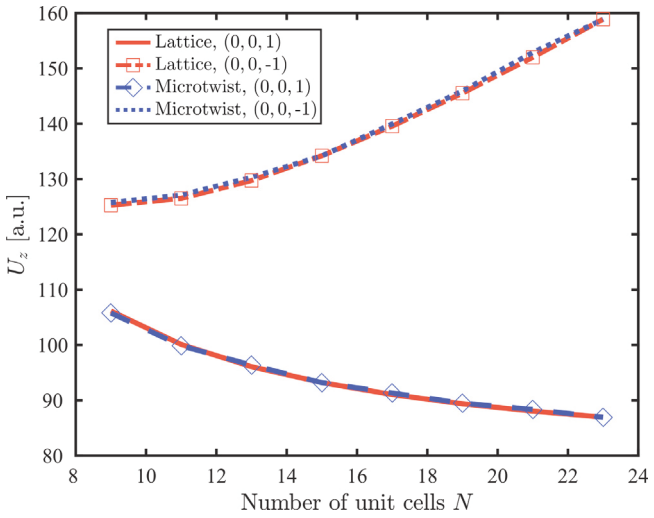

Fig. 9. Simulated indentation responses for polarized Pyrochlore lattice of different number of unit cells.

5. Conclusion

In this paper, we develop a 3D microtwist elasticity to capture the zero modes and topological polarization of Pyrochlore lattices on a macroscopic scale. The essence of the approach is based on a two-scale asymptotic homogenization approach by introducing additional DOFs to map non-trivial zero modes of twisting motions. Performance of the proposed theory is validated against the discrete model in a number of problems including determining the P-asymmetric distribution of zero modes, calculating the dispersion relations and quantitatively predicting the polarized indentation response of finite samples. Thus, by placing P-asymmetric zero modes in the heart of the theory, the study should bring a fresh understanding of the polarized statics and dynamics of architected materials in particular, and of microstructured media more generally.

The theory extends easily to nearly-isostatic Pyrochlore lattices, i.e., with next-nearest-neighbor interactions or elasticity in the hinges, as long as the elastic constants of the bonds breaking isostaticity are kept small. It also extends to other isostatic lattices with multiple periodic zero modes that are on the brink of a regular-distorted, or polarized-unpolarized, phase transition. In the future, if we directly adopt the microtwist theory to interpret non-trivial periodic zero modes in other isostatic lattices, we believe the homogenization based on the strain energy approach is an option to consider. Hopefully, the 3D microtwist continuum theory will be implemented to solve materials inverse design problems by optimizing the lattice microstructures to match the effective constants that have been found to achieve the desired mechanical polarization functionalities.

CRediT authorship contribution statement

Rongyu Xia: Formal analysis, Performing simulations, Writing. **Hussein Nassar:** Formal analysis, Methodology, Funding acquisition. **Hui Chen:** Conceptualization, Formal analysis, Methodology, Performing simulations, Writing. **Zheng Li:** Validation, Writing. **Guoliang Huang:** Conceptualization, Validation, Supervision, Funding acquisition, Writing.

Declaration of competing interest

The authors declare that they have no known competing financial interests or personal relationships that could have appeared to influence the work reported in this paper.

Acknowledgments

This work is supported by the NSF CMMI, USA under Award No. 1930873 with Program Manager Dr. Nakhiah Goulbourne, the Air Force Office of Scientific Research, USA under Grant No. AF 9550-18-1-0342 and AF 9550-20-0279 with Program Manager Dr. Byung-Lip (Les) Lee and the Army Research Office, USA under Grant No. W911NF-18-1-0031 with Program Manager Dr. Daniel P. Cole. Rongyu Xia is grateful for the support from China Scholarship Council.

Appendix A. Influence of elasticity in the hinges

The expression of the compatibility matrix corresponding to the next-nearest-neighbor bonds is

$$C_H = \begin{bmatrix}
-\mathbf{e}'_{11} & \mathbf{0} & \mathbf{e}'_{11} & \mathbf{0} \\
-\mathbf{e}'_{12} & \mathbf{0} & \mathbf{0} & \mathbf{e}'_{12} \\
-\mathbf{e}'_{13} & \mathbf{e}'_{13} & \mathbf{0} & \mathbf{0} \\
-\mathbf{e}'_{14} & \mathbf{0} & \mathbf{0} & \mathbf{e}'_{14} \\
-\mathbf{e}'_{15} & \mathbf{e}'_{15} & \mathbf{0} & \mathbf{0} \\
-\mathbf{e}'_{16} & \mathbf{0} & \mathbf{e}'_{16} & \mathbf{0} \\
\mathbf{e}'_{21} & -\mathbf{e}'_{21} & \mathbf{0} & \mathbf{0} \\
\mathbf{0} & -\mathbf{e}'_{22} & \mathbf{0} & \mathbf{e}'_{22} \\
\mathbf{e}'_{23} & -\mathbf{e}'_{23} & \mathbf{0} & \mathbf{0} \\
\mathbf{0} & -\mathbf{e}'_{24} & \mathbf{e}'_{24} & \mathbf{0} \\
\mathbf{0} & -\mathbf{e}'_{25} & \mathbf{e}'_{25} & \mathbf{0} \\
\mathbf{0} & -\mathbf{e}'_{26} & \mathbf{0} & \mathbf{e}'_{26} \\
\mathbf{e}'_{31} & \mathbf{0} & -\mathbf{e}'_{31} & \mathbf{0} \\
\mathbf{0} & \mathbf{e}'_{32} & -\mathbf{e}'_{32} & \mathbf{0} \\
\mathbf{0} & \mathbf{e}'_{33} & -\mathbf{e}'_{33} & \mathbf{0} \\
\mathbf{0} & \mathbf{0} & -\mathbf{e}'_{34} & \mathbf{e}'_{34} \\
\mathbf{e}'_{35} & \mathbf{0} & -\mathbf{e}'_{35} & \mathbf{0} \\
\mathbf{0} & \mathbf{0} & -\mathbf{e}'_{36} & \mathbf{e}'_{36} \\
\mathbf{0} & \mathbf{e}'_{41} & \mathbf{0} & -\mathbf{e}'_{41} \\
\mathbf{0} & \mathbf{0} & \mathbf{e}'_{42} & -\mathbf{e}'_{42} \\
\mathbf{e}'_{43} & \mathbf{0} & \mathbf{0} & -\mathbf{e}'_{43} \\
\mathbf{0} & \mathbf{0} & \mathbf{e}'_{44} & -\mathbf{e}'_{44} \\
\mathbf{e}'_{45} & \mathbf{0} & \mathbf{0} & -\mathbf{e}'_{45} \\
\mathbf{0} & \mathbf{e}'_{46} & \mathbf{0} & -\mathbf{e}'_{46}
\end{bmatrix}, \quad \begin{aligned}
\mathbf{e}'_{11} &= \left(a_1\mathbf{m}_1 - b_4\mathbf{m}_4\right) / \left\|a_1\mathbf{m}_1 - b_4\mathbf{m}_4\right\|, \\
\mathbf{e}'_{12} &= \left(a_1\mathbf{m}_1 + b_6\mathbf{m}_6\right) / \left\|a_1\mathbf{m}_1 + b_6\mathbf{m}_6\right\|, \\
\mathbf{e}'_{13} &= \left(a_2\mathbf{m}_2 + b_4\mathbf{m}_4\right) / \left\|a_2\mathbf{m}_2 + b_4\mathbf{m}_4\right\|, \\
\mathbf{e}'_{14} &= \left(a_2\mathbf{m}_2 - b_5\mathbf{m}_5\right) / \left\|a_2\mathbf{m}_2 - b_5\mathbf{m}_5\right\|, \\
\mathbf{e}'_{15} &= \left(a_3\mathbf{m}_3 - b_6\mathbf{m}_6\right) / \left\|a_3\mathbf{m}_3 - b_6\mathbf{m}_6\right\|, \\
\mathbf{e}'_{16} &= \left(a_3\mathbf{m}_3 + b_5\mathbf{m}_5\right) / \left\|a_3\mathbf{m}_3 + b_5\mathbf{m}_5\right\|, \\
\mathbf{e}'_{21} &= \left(a_4\mathbf{m}_4 + b_2\mathbf{m}_2\right) / \left\|a_4\mathbf{m}_4 + b_2\mathbf{m}_2\right\|, \\
\mathbf{e}'_{22} &= \left(a_4\mathbf{m}_4 - b_5\mathbf{m}_5\right) / \left\|a_4\mathbf{m}_4 - b_5\mathbf{m}_5\right\|, \\
\mathbf{e}'_{23} &= \left(-a_6\mathbf{m}_6 + b_3\mathbf{m}_3\right) / \left\|a_6\mathbf{m}_6 - b_3\mathbf{m}_3\right\|, \\
\mathbf{e}'_{24} &= \left(-a_6\mathbf{m}_6 + b_5\mathbf{m}_5\right) / \left\|a_6\mathbf{m}_6 - b_5\mathbf{m}_5\right\|, \\
\mathbf{e}'_{25} &= \left(-a_1\mathbf{m}_1 - b_2\mathbf{m}_2\right) / \left\|a_1\mathbf{m}_1 + b_2\mathbf{m}_2\right\|, \\
\mathbf{e}'_{26} &= \left(-a_1\mathbf{m}_1 - b_3\mathbf{m}_3\right) / \left\|a_1\mathbf{m}_1 + b_3\mathbf{m}_3\right\|, \\
\mathbf{e}'_{31} &= \left(a_5\mathbf{m}_5 + b_3\mathbf{m}_3\right) / \left\|a_5\mathbf{m}_5 + b_3\mathbf{m}_3\right\|, \\
\mathbf{e}'_{32} &= \left(a_5\mathbf{m}_5 - b_6\mathbf{m}_6\right) / \left\|a_5\mathbf{m}_5 - b_6\mathbf{m}_6\right\|, \\
\mathbf{e}'_{33} &= \left(-a_2\mathbf{m}_2 - b_1\mathbf{m}_1\right) / \left\|a_2\mathbf{m}_2 + b_1\mathbf{m}_1\right\|, \\
\mathbf{e}'_{34} &= \left(-a_2\mathbf{m}_2 - b_3\mathbf{m}_3\right) / \left\|a_2\mathbf{m}_2 + b_3\mathbf{m}_3\right\|, \\
\mathbf{e}'_{35} &= \left(-a_4\mathbf{m}_4 + b_1\mathbf{m}_1\right) / \left\|a_4\mathbf{m}_4 - b_1\mathbf{m}_1\right\|, \\
\mathbf{e}'_{36} &= \left(-a_4\mathbf{m}_4 + b_6\mathbf{m}_6\right) / \left\|a_4\mathbf{m}_4 - b_6\mathbf{m}_6\right\|, \\
\mathbf{e}'_{41} &= \left(-a_3\mathbf{m}_3 - b_1\mathbf{m}_1\right) / \left\|a_3\mathbf{m}_3 + b_1\mathbf{m}_1\right\|, \\
\mathbf{e}'_{42} &= \left(-a_3\mathbf{m}_3 - b_2\mathbf{m}_2\right) / \left\|a_3\mathbf{m}_3 + b_2\mathbf{m}_2\right\|, \\
\mathbf{e}'_{43} &= \left(a_6\mathbf{m}_6 + b_1\mathbf{m}_1\right) / \left\|a_6\mathbf{m}_6 + b_1\mathbf{m}_1\right\|, \\
\mathbf{e}'_{44} &= \left(a_6\mathbf{m}_6 - b_4\mathbf{m}_4\right) / \left\|a_6\mathbf{m}_6 - b_4\mathbf{m}_4\right\|, \\
\mathbf{e}'_{45} &= \left(-a_5\mathbf{m}_5 + b_2\mathbf{m}_2\right) / \left\|a_5\mathbf{m}_5 - b_2\mathbf{m}_2\right\|, \\
\mathbf{e}'_{46} &= \left(-a_5\mathbf{m}_5 + b_4\mathbf{m}_4\right) / \left\|a_5\mathbf{m}_5 - b_4\mathbf{m}_4\right\|.
\end{aligned} \tag{A.1}$$

Appendix B. Supplementary data

Supplementary material related to this article can be found online at https://doi.org/10.1016/j.jmps.2021.104564.

References

Baardink, G., Souslov, A., Paulose, J., Vitelli, V., 2018. Localizing softness and stress along loops in 3D topological metamaterials. Proc. Natl. Acad. Sci. U.S.A 115, 489–494.
Bilal, O.R., Süsstrunk, C., Huber, S.D., 2017. Intrinsically polar elastic metamaterials. Adv. Mater. 29, 1700540.
Cosserat, E., Cosserat, F., 1909. Théorie Des Corps Déformables. Hermann, Paris.
Deshpande, V.S., Fleck, N.A., Ashby, M.F., 2001. Effective properties of the octet-truss lattice material. J. Mech. Phys. Solids 49, 1747–1769.
Hutchinson, R.G., Fleck, N.A., 2006. The structural performance of the periodic truss. J. Mech. Phys. Solids 54, 756–782.
Kadic, M., Bückmann, N., Thiel, M., Wegener, M., 2012. On the practicability of pentamode mechanical metamaterials. Appl. Phys. Lett. 100, 191901.
Kane, C.L., Lubensky, T.C., 2014. Topological boundary modes in isostatic lattices. Nat. Phys. 10, 39–45.
Lubensky, T.C., Kane, C.L., Mao, X.M., Souslov, A., Sun, K., 2015. Phonons and elasticity in critically coordinated lattices. Rep. Prog. Phys. 78, 109501.

Ma, J.H., Zhou, D., Sun, K., Mao, X.M., Gonella, S., 2018. Edge modes and asymmetric wave transport in topological lattices: experimental characterization at finite frequencies. Phys. Rev. Lett. 121, 094301.
Mao, X.M., Lubensky, T.C., 2018. Maxwell lattices and topological mechanics. Annu. Rev. Condens. Matter Phys. 9, 413–433.
Milton, G.W., 2013. Complete characterization of the macroscopic deformations of periodic unimode metamaterials of rigid bars and pivots. J. Mech. Phys. Solids 61, 1543–1560.
Milton, G.W., Cherkaev, A.V., 1995. Which elasticity tensors are realizable? J. Eng. Mater. Technol. 117, 483–493.
Nassar, H., Chen, Y., Huang, G.L., 2018a. A degenerate polar lattice for cloaking in full two-dimensional elastodynamics and statics. Proc. R. Soc. Lond. Ser. A Math. Phys. Eng. Sci. 474, 20180523.
Nassar, H., Chen, Y.Y., Huang, G.L., 2019. Isotropic polar solids for conformal transformation elasticity and cloaking. J. Mech. Phys. Solids 129, 229–243.
Nassar, H., Chen, Y.Y., Huang, G.L., 2020a. Polar metamaterials : A new outlook on resonance for cloaking applications. Phys. Rev. Lett. 124, 84301.
Nassar, H., Chen, H., Huang, G.L., 2020b. Microtwist elasticity: A continuum approach to zero modes and topological polarization in Kagome lattices. J. Mech. Phys. Solids 144, 104107.
Norris, A.N., Shuvalov, A.L., 2011. Elastic cloaking theory. Wave Motion 48, 525–538.
Rocklin, D.Z., 2017. Directional mechanical response in the bulk of topological metamaterials. New J. Phys. 19, 065004.
Rocklin, D.Z., Zhou, S.N., Sun, K., Mao, X.M., 2017. Transformable topological mechanical metamaterials. Nat. Commun. 8, 14201.
Saremi, A., Rocklin, D.Z., 2020. Topological elasticity of flexible structures. Phys. Rev. X 10, 011052.
Stenull, O., Kane, C.L., Lubensky, T.C., 2016. Topological phonons and Weyl lines in three dimensions. Phys. Rev. Lett. 117, 068001.
Stenull, O., Lubensky, T.C., 2019. Signature of topological phonons in superisostatic lattices. Phys. Rev. Lett. 122, 248002.
Sun, K., Mao, X., 2020. Continuum theory for topological edge soft modes. Phys. Rev. Lett. 124, 207601.
Sun, K., Souslov, A., Mao, X.M., Lubensky, T.C., 2012. Surface phonons, elastic response, and conformal invariance in twisted kagome lattices. Proc. Natl. Acad. Sci. U.S.A 109, 12369–12374.
Xu, X., Wang, C., Shou, W., Du, Z., Chen, Y., Li, B., Matusik, W., Nassar, H., Huang, G.L., 2020. Physical realization of elastic cloaking with a polar material. Phys. Rev. Lett. 124, 114301.
Zhang, H.K., Chen, Y., Liu, X.N., Hu, G.K., 2020. An asymmetric elastic metamaterial model for elastic wave cloaking. J. Mech. Phys. Solids 135, 103796.
Zhang, L.Y., Mao, X.M., 2018. Fracturing of topological Maxwell lattices. New J. Phys. 20, 063034.